



# NAVAL POSTGRADUATE SCHOOL

MONTEREY, CALIFORNIA

## THESIS

### INVESTIGATION OF COHERENT AND INCOHERENT CHANGE DETECTION ALGORITHMS

by

Nicholas S. Underwood

December 2017

Thesis Advisor:  
Co-Advisor:  
Second Reader:

David A. Garren  
Pete Mastin  
Ric Romero

**Approved for public release. Distribution is unlimited.**

THIS PAGE INTENTIONALLY LEFT BLANK

<b>REPORT DOCUMENTATION PAGE</b>			<i>Form Approved OMB No. 0704-0188</i>	
Public reporting burden for this collection of information is estimated to average 1 hour per response, including the time for reviewing instruction, searching existing data sources, gathering and maintaining the data needed, and completing and reviewing the collection of information. Send comments regarding this burden estimate or any other aspect of this collection of information, including suggestions for reducing this burden, to Washington headquarters Services, Directorate for Information Operations and Reports, 1215 Jefferson Davis Highway, Suite 1204, Arlington, VA 22202-4302, and to the Office of Management and Budget, Paperwork Reduction Project (0704-0188) Washington DC 20503.				
<b>1. AGENCY USE ONLY</b> (Leave blank)		<b>2. REPORT DATE</b> December 2017		<b>3. REPORT TYPE AND DATES COVERED</b> Master's thesis
<b>4. TITLE AND SUBTITLE</b> INVESTIGATION OF COHERENT AND INCOHERENT CHANGE DETECTION ALGORITHMS			<b>5. FUNDING NUMBERS</b>	
<b>6. AUTHOR(S)</b> Nicholas S. Underwood				
<b>7. PERFORMING ORGANIZATION NAME(S) AND ADDRESS(ES)</b> Naval Postgraduate School Monterey, CA 93943-5000			<b>8. PERFORMING ORGANIZATION REPORT NUMBER</b>	
<b>9. SPONSORING /MONITORING AGENCY NAME(S) AND ADDRESS(ES)</b> N/A			<b>10. SPONSORING / MONITORING AGENCY REPORT NUMBER</b>	
<b>11. SUPPLEMENTARY NOTES</b> The views expressed in this thesis are those of the author and do not reflect the official policy or position of the Department of Defense or the U.S. Government. IRB number ____N/A____.				
<b>12a. DISTRIBUTION / AVAILABILITY STATEMENT</b> Approved for public release. Distribution is unlimited.			<b>12b. DISTRIBUTION CODE</b>	
<b>13. ABSTRACT (maximum 200 words)</b>  An investigation of five change detection methods used in synthetic aperture radar (SAR) is presented in this thesis. This investigation utilizes data gathered from the Air Force Research Laboratory (AFRL) Sensor Data Management System (SDMS) in order to compare the various change detection techniques. These change detection methods include the following: a) incoherent change detection (ICCD), b) coherent change detection (CCD), c) alternative coherent change detection (ACCD), d) log likelihood change statistic (LLCS), and e) a two-stage change detection, which involves a combination of ICCD and CCD. In addition, a new change detection method for comparison with these five basic methods is developed. This investigation reveals that the LLCS statistic is the most promising method for revealing changes within the SDMS dataset. Furthermore, the author's change detection method yields overall visual improvement in comparison to the two-stage change detection method.				
<b>14. SUBJECT TERMS</b> synthetic aperture radar, coherent change detection, incoherent change detection			<b>15. NUMBER OF PAGES</b> 77	
			<b>16. PRICE CODE</b>	
<b>17. SECURITY CLASSIFICATION OF REPORT</b> Unclassified	<b>18. SECURITY CLASSIFICATION OF THIS PAGE</b> Unclassified	<b>19. SECURITY CLASSIFICATION OF ABSTRACT</b> Unclassified	<b>20. LIMITATION OF ABSTRACT</b> UU	

NSN 7540-01-280-5500

Standard Form 298 (Rev. 2-89)  
Prescribed by ANSI Std. Z39-18

THIS PAGE INTENTIONALLY LEFT BLANK

**Approved for public release. Distribution is unlimited.**

**INVESTIGATION OF COHERENT AND INCOHERENT CHANGE  
DETECTION ALGORITHMS**

Nicholas S. Underwood  
Civilian, NAVAIR  
B.S., University of Michigan, Ann Arbor, 2010

Submitted in partial fulfillment of the  
requirements for the degree of

**MASTER OF SCIENCE IN ELECTRICAL ENGINEERING**

from the

**NAVAL POSTGRADUATE SCHOOL  
December 2017**

Approved by: David A. Garren  
Thesis Advisor

Pete Mastin  
BTP Systems  
Co-Advisor

Ric Romero  
Second Reader

R. Clark Robertson  
Chair, Department of Electrical and Computer Engineering

THIS PAGE INTENTIONALLY LEFT BLANK

## **ABSTRACT**

An investigation of five change detection methods used in synthetic aperture radar (SAR) is presented in this thesis. This investigation utilizes data gathered from the Air Force Research Laboratory (AFRL) Sensor Data Management System (SDMS) in order to compare the various change detection techniques. These change detection methods include the following: a) incoherent change detection (ICCD), b) coherent change detection (CCD), c) alternative coherent change detection (ACCD), d) log likelihood change statistic (LLCS), and e) a two-stage change detection, which involves a combination of ICCD and CCD. In addition, a new change detection method for comparison with these five basic methods is developed. This investigation reveals that the LLCS statistic is the most promising method for revealing changes within the SDMS dataset. Furthermore, the author's change detection method yields overall visual improvement in comparison to the two-stage change detection method.

THIS PAGE INTENTIONALLY LEFT BLANK



## TABLE OF CONTENTS

<b>I.</b>	<b>INTRODUCTION.....</b>	<b>1</b>
<b>A.</b>	<b>PURPOSE OF THESIS.....</b>	<b>1</b>
<b>B.</b>	<b>THESIS ORGANIZATION.....</b>	<b>2</b>
<b>II.</b>	<b>SAR CONCEPTS AND DESCRIPTIONS.....</b>	<b>3</b>
<b>A.</b>	<b>SDMS DATA.....</b>	<b>3</b>
<b>B.</b>	<b>MATHEMATICAL CONCEPTS.....</b>	<b>4</b>
1.	Spatial Averaging (Moving Window).....	4
2.	Correlation.....	5
3.	Covariance.....	5
<b>C.</b>	<b>SAR CONCEPTS.....</b>	<b>6</b>
1.	Speckle.....	6
2.	Backscatter Power.....	7
3.	Coherence.....	8
4.	Polarization.....	8
5.	Repeat Pass.....	10
<b>III.</b>	<b>CHANGE DETECTION.....</b>	<b>11</b>
<b>A.</b>	<b>INCOHERENT CHANGE DETECTION.....</b>	<b>12</b>
<b>B.</b>	<b>COHERENT CHANGE DETECTION.....</b>	<b>12</b>
<b>C.</b>	<b>ALTERNATIVE COHERENT CHANGE DETECTION.....</b>	<b>13</b>
<b>D.</b>	<b>LOG LIKELIHOOD CHANGE STATISTIC.....</b>	<b>13</b>
<b>E.</b>	<b>TWO-STAGE COHERENT CHANGE DETECTION.....</b>	<b>15</b>
<b>IV.</b>	<b>THREE-STAGE CHANGE DETECTION.....</b>	<b>19</b>
<b>A.</b>	<b>K-MEANS CLUSTERING.....</b>	<b>20</b>
<b>B.</b>	<b>EXTENDED LLCS FILTER.....</b>	<b>21</b>
<b>C.</b>	<b>BINARY OPERATIONS.....</b>	<b>23</b>
1.	Binary Thresholding.....	23
2.	Binary Integration.....	23
<b>V.</b>	<b>CHANGE DETECTION SIMULATION RESULTS.....</b>	<b>27</b>
<b>A.</b>	<b>SIMULATOR MODEL AND PARAMETERS.....</b>	<b>27</b>
<b>B.</b>	<b>SIMULATOR RESULTS.....</b>	<b>29</b>
<b>VI.</b>	<b>CHANGE DETECTOR INVESTIGATION.....</b>	<b>35</b>
<b>A.</b>	<b>DESCRIPTION OF THE AREA OF INTEREST.....</b>	<b>36</b>

B.	GROUND TRUTH.....	36
C.	ICCD VERSUS CCD RESULTS.....	39
D.	ACCD VERSUS CCD RESULTS .....	43
E.	LLCS RESULTS.....	46
F.	TWO-STAGE RESULTS.....	49
G.	THREE-STAGE CHANGE DETECTION RESULTS.....	53
VII.	CONCLUSIONS .....	55
A.	DISCUSSION OF RESULTS .....	55
B.	FUTURE WORK.....	55
	LIST OF REFERENCES .....	57
	INITIAL DISTRIBUTION LIST .....	59

## LIST OF FIGURES

Figure 1.	CCD Challenge Problem Scene. Source: [8].	4
Figure 2.	Zoomed-in Area of CCD Challenge Dataset	6
Figure 3.	Over-filtered Image of a Building in the CCD Challenge Dataset	7
Figure 4.	Antennas Oriented in VV Polarization	9
Figure 5.	Antennas Oriented in HH Polarization	9
Figure 6.	Antennas Orientated in HV Polarization	10
Figure 7.	General Change Detection Algorithm Flowchart	11
Figure 8.	Two-Stage Change Detection Flowchart. Adapted from [6].	16
Figure 9.	Probability Space of $H_0$ and $H_1$ Hypotheses for Two-Stage Change Detection. Source: [6].	17
Figure 10.	Three-Stage Change Detection Flowchart	19
Figure 11.	Application of $K$ -Means Algorithm	20
Figure 12.	CCD Challenge Problem Dataset with $K$ -Means Application	21
Figure 13.	Extended LLCS and Segmentation Process Flowchart	22
Figure 14.	Binary Integrator Neighborhood Example	24
Figure 15.	Pre- and Post-binary Integrator Images	25
Figure 16.	Focused Red Area of Figure 15	25
Figure 17.	Change Detection Simulator Flowchart	27
Figure 18.	ICCD Simulated versus Theoretical Results	29
Figure 19.	CCD Simulated versus Theoretical Results	30
Figure 20.	Simulated Constant Power LLCS versus Theoretical Results	31
Figure 21.	Simulated Constant Coherence LLCS versus Theoretical Results	33
Figure 22.	Mission and Reference Images of Area of Interest	36

Figure 23.	Mission Image Comparison to Ground Truth.....	37
Figure 24.	Ground Truth versus Extended Guard Cells.....	38
Figure 25.	Zoomed-in Area of Suspected Car.....	39
Figure 26.	ICCD and CCD Subarea Results .....	40
Figure 27.	Track Area of Figure 26.....	40
Figure 28.	Zoomed-in Car Area of Figure 26 .....	41
Figure 29.	ROC Curve for ICCD versus CCD.....	42
Figure 30.	ICCD versus CCD Binary Change Maps with Ground Truth .....	42
Figure 31.	Area of Interest with ACCD versus CCD Raw Outputs.....	43
Figure 32.	Zoomed-in Car Area ACCD versus CCD Change Detection Methods.....	44
Figure 33.	ROC Curve for ACCD versus CCD .....	45
Figure 34.	ACCD versus CCD Binary Change Maps with Ground Truth.....	46
Figure 35.	LLCS versus CCD versus ICCD Single Car Results.....	47
Figure 36.	ROC Curves for CCD versus ICCD versus LLCS .....	48
Figure 37.	Change Detection ROCs. Source: [20]. .....	49
Figure 38.	ACCD versus Two-Stage Raw Output .....	49
Figure 39.	ACCD versus Two-Stage Track Areas.....	50
Figure 40.	ACCD versus Two-Stage Car Areas.....	51
Figure 41.	ROC Curves of ACCD, ICCD, and Two-Stage Filters .....	51
Figure 42.	ACCD and Two-Stage Comparison to Ground Truth .....	52
Figure 43.	LLCS versus Three-Stage LLCS Output .....	53
Figure 44.	ROC Curves for LLCS versus Three Stage .....	54
Figure 45.	Change Masks of Three Stage, Two Stage Change Mask, and Ground Truth .....	54

## LIST OF TABLES

Table 1.	AFRL SAR Sensor Parameters. Adapted from [8].	35
Table 2.	Average Object Dimensions. Adapted from [17], [18].	35

THIS PAGE INTENTIONALLY LEFT BLANK

## LIST OF ACRONYMS AND ABBREVIATIONS

AFRL	Air Force Research Laboratory
ACCD	Alternative Coherent Change Detection
CCD	Coherent Change Detection
HH	Horizontal-Horizontal
HV	Horizontal-Vertical
ICCD	Incoherent Change Detection
LLCS	Log Likelihood Change Statistic
MATLAB	Mathematics Laboratory Software
$P_d$	Probability of Detection
PDF	Probability Density Function
$P_{fa}$	Probability of False Alarm
ROC	Receiver Operating Characteristic
SAR	Synthetic Aperture Radar
SDMS	Sensor Data Management System
VV	Vertical-Vertical

THIS PAGE INTENTIONALLY LEFT BLANK



## **ACKNOWLEDGMENTS**

I thank Professor Garren, Pete, and Cho for their aid and insight in helping me in developing this thesis. It has been a privilege, to say the least.

I also thank my girlfriend, Candice. Without her encouragement and belief in me, I do not believe I would be where I am today. In addition, I wanted to thank Adam Andersen and NAVAIR for their support of my master's education.

THIS PAGE INTENTIONALLY LEFT BLANK

# **I. INTRODUCTION**

Synthetic aperture radar (SAR) is a radar application that can image large geographical areas and detect changes in the scene. This concept was introduced by Carl Wiley in 1951 and showed the manner in which a large geographical area, e.g., one square mile, can be captured and imaged without the need of a large antenna aperture [1]. As research progressed with SAR, applications became more sophisticated. SAR methods were developed including the following applications: a) capturing seismic effects in localized regions [2], b) monitoring ship traffic around ports [3], and c) measuring displacements of cargo containers inside shipyards [4]. Each of these examples applies the concepts of change detection. Change detection methodologies are the focus of this thesis.

There are two general modalities of change detection: incoherent and coherent. Incoherent change detection typically involves comparing the mean intensities of two or more images region [5]. The resulting intensities can be affected by noise of the receiver or a change in the scene, as if a car moved out of a parking spot or a tractor plowed through a field. Coherent change detection is different from the non-coherent methods in that the phase information is used, which allows for improved detection of small-scale changes [6].

In this thesis, we investigate a number of varieties of both incoherent and change detection methods. In two special cases, we examine methods resulting from a combination of two or more of the basic change detection methods.

## **A. PURPOSE OF THESIS**

The purpose of this thesis is to investigate and understand basic change detection methods. In order to facilitate this analysis, a dataset obtained from Air Force Research Laboratory (AFRL) is processed using the different change detection schemes. The database that AFRL offers is called the Sensor Data Management System (SDMS) database. The available SDMS data includes different SAR platforms' collections at different geographical locations as well as various simulated target datasets. The dataset

chosen for the present investigation is the coherent change detection (CCD) Challenge Problem. This dataset is described in more detail in Chapter II Section A.

In this investigation, we present the results of six different change detection methods. The author developed the concepts of the sixth and final method examined. Each of the candidate methods are applied to the SDMS data and then evaluated based on visually-derived ground truth and receiver operating characteristic (ROC) curves.

## **B. THESIS ORGANIZATION**

The thesis is organized in a manner to describe the concepts, simulate the models, and apply the concepts and models to real-world data. A brief explanation on SAR and mathematical concepts are covered in Chapter II. This includes concepts of backscatter power and coherence, which are two of the key metrics of interest in this investigation. The types of change detection methods studied in this investigation are shown in Chapter III. This includes equations and descriptions of each method's change metrics. Design and concepts of an improvised change detection method is presented in Chapter IV. The simulator design and simulation results are covered in Chapter V. The change detection methods are applied to SDMS dataset in Chapter VI. Finally, the discussion of results and future work is covered in Chapter VII.

## II. SAR CONCEPTS AND DESCRIPTIONS

In this chapter, we provide an introduction to the SDMS data, which are utilized in the discussion of the various change detection algorithms. In addition, in this section is provided a discussion of the relevant mathematical concepts and the SAR principles.

### A. SDMS DATA

The available SDMS datasets [7] cover a number of relevant images, including: a) simulated SAR targets, b) targets imbedded in forest terrain, c) moving targets within an urban environment, d) time-lapsed photos of a set scene, and e) multiple others. There are various challenges that are developed for each of the datasets. In this thesis, we concentrate on the methods of change detection, so a relevant dataset was chosen to accommodate this focus—the CCD challenge problem [8]. The image of the entire scene in the CCD challenge dataset is shown in Figure 1.

The subfigures shown in Figure 1 are labeled as mission, reference, and CCD. The mission subfigure is a baseline scene image captured at a certain time interval. The reference subfigure is the same scene image captured at a later time interval. The CCD subfigure shows the CCD’s change metric image. In the CCD subfigure, there are labels showing objects in the figure. This is the only “truth data” provided in the CCD challenge problem dataset.

The datasets have two different types of data available: real and complex. The CCD challenge problem dataset is multi-polarized and complex-valued data. When investigating the incoherent change detection scheme, we take the absolute value of the complex data to mimic only magnitude data. All other change detection methods in this paper are able to process complex data.



Figure 1. CCD Challenge Problem Scene. Source: [8].

## B. MATHEMATICAL CONCEPTS

### 1. Spatial Averaging (Moving Window)

SAR data usually has noise and speckle artifacts contained within the imagery and is a natural phenomenon of the SAR image formation process. A method of spatial averaging, which is also named the “moving window” technique, can reduce the speckle and filter the high frequency noise in the SAR data. The archetypical equation for the moving window is

$$I = \frac{1}{N} \sum_{k=1}^N I_k, \quad (1)$$

where  $I_k$  is the  $k$ th pixel intensity and  $N$  is the total number of image cells of interest. This moving window resembles a low-pass filter which attenuates high frequency noise energy.

## 2. Correlation

Correlation is a measure to check for linear dependence between two random variables. The only drawback of correlation is that it does not imply causation; thus, two random variables can appear to be correlated. If one random variable begins to vary, an effect may not be evident in the other random variables. The correlation coefficient equation is given by

$$|\rho_{x,y}| = \frac{E\{xy^*\} - m_x m_y^*}{\sigma_x \sigma_y}. \quad (2)$$

Here,  $E\{xy^*\}$  represents the expected value of the product of the  $x$  random variable and the conjugate of the  $y$  random variable. In addition,  $m_x$  and  $m_y$  represent the means of the  $x$  and  $y$  random variables, respectively, and the  $\sigma_x$  and  $\sigma_y$  represent the standard deviations of the  $x$  and  $y$  random variables, respectively. The correlation coefficient magnitude  $|\rho_{x,y}|$  has values which range from zero to unity. Two random variables are said to be correlated if the correlation coefficient magnitude is near unity. Two random variables are said to be uncorrelated if this magnitude is approximately zero.

## 3. Covariance

Covariance is a measure of how the product of two mean-removed random variables trend in behavior. For example, if the random variable  $x$  is increasing and that of  $y$  is increasing, then these random variables are said to vary with one another. The means must be removed from the respective random variables in order to capture the appropriate measure of this behavior

$$\gamma_{x,y} = E\{(x - m_x)(y - m_y)^H\}. \quad (3)$$

Here,  $E\{:\}$  is the expected value of the complex conjugate,  $x$  and  $y$  are random variables,  $m_x$  and  $m_y$  represent the means of the  $x$  and  $y$  random variables, respectively, and  $(:)^H$  represents the Hermitian transpose.

The Hermitian transpose is the conjugate transpose of an array or matrix. This is specific to complex data. For real-valued data, the Hermitian transpose is replaced with a transpose.

## C. SAR CONCEPTS

### 1. Speckle

Examination of SAR imagery reveals that there are typically artifacts which appear across each image. These “speckle” artifacts are due to multiple diffractions and reflections occurring from rough surfaces. An example image containing such speckle is presented in Figure 2. This phenomenon becomes apparent in Chapter VI when examining with the SDMS data. Furthermore, the type of change detection being performed can mitigate or exasperate the effects of speckle. Speckle is regarded as multiplicative noise in SAR applications [9].

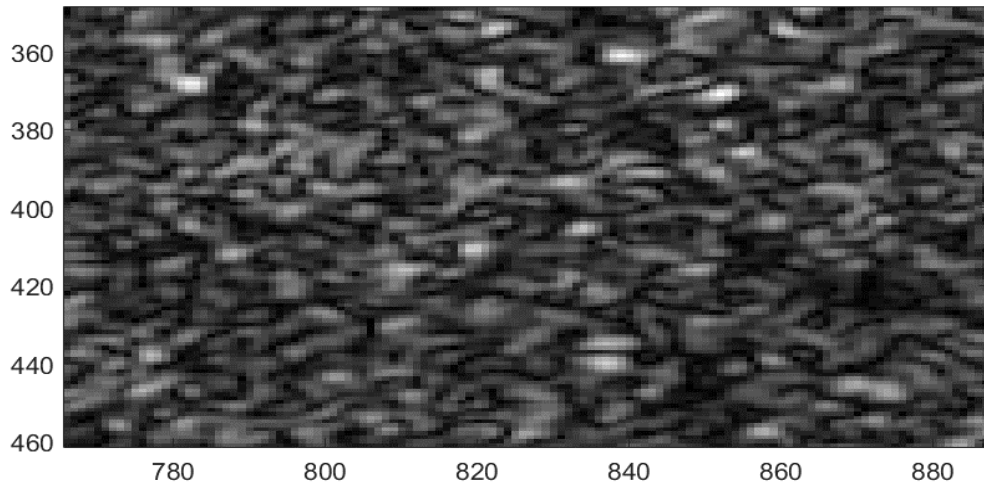


Figure 2. Zoomed-in Area of CCD Challenge Dataset

Inherently, speckle has high frequency components. These high frequency components can cause errors when performing CCD and can lead to false alarms in detection. Spatial averaging performs low pass filtering that reduces the amount of high frequency content in the image; however, such averaging can reduce the ability to resolve



object edges by blending them into the background. An example of this blending of edges is presented in Figure 3. The scene in Figure 3 was identified as a building [8]. This scene was averaged using a 15 by 15 moving window.

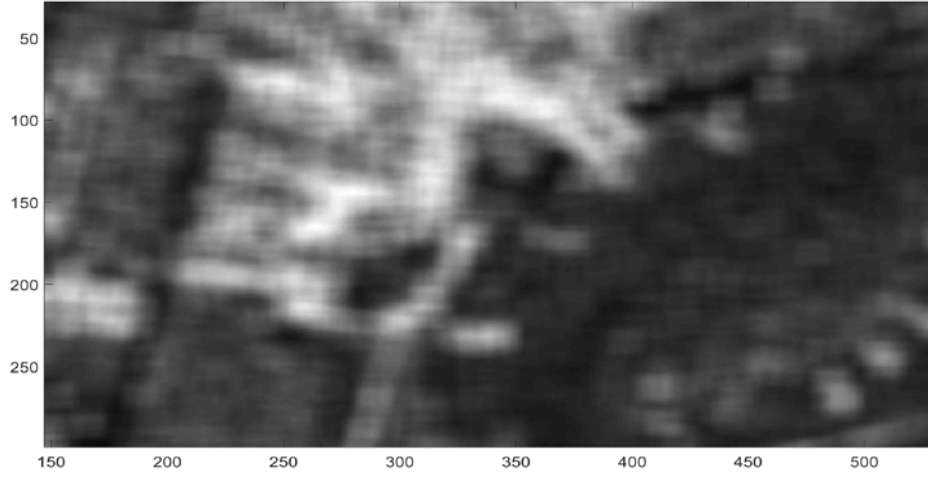


Figure 3. Over-filtered Image of a Building in the CCD Challenge Dataset

## 2. Backscatter Power

In this thesis, the term “backscatter power” is a reference to the estimate of backscatter power, as opposed to the true backscatter power of a scene. The existence of speckle corrupts local groups of pixels and, thus, requires averaging to filter out some of the speckle effect [9]. Mathematically, this process is represented as

$$I = \frac{1}{N} \sum_{k=1}^N |f_k|^2. \quad (4)$$

The variable  $N$  is the number of pixels being in the local neighborhood,  $|f_k|^2$  is the absolute value of the pixel amplitude squared, and  $I$  is the estimate of the mean backscatter power.

### 3. Coherence

The term coherence in this thesis refers to the stability of the phase from one image pixel to the next. If the phase varies randomly, then the various methods which use CCD are impacted. The factors that affect coherence are revealed in the product

$$\gamma = \gamma_{SNR} \gamma_{base} \gamma_{scene} \gamma_{vol} \gamma_{proc} . \quad (5)$$

Here,  $\gamma_{SNR}$  is decorrelation due to receiver sensitivity,  $\gamma_{base}$  is decorrelation from the inability of the aircraft to replicate the previous pass exactly,  $\gamma_{scene}$  is the decorrelation from contributions of multiple scattering centers in a scene,  $\gamma_{vol}$  decorrelation due to scattering from rough surfaces, and  $\gamma_{proc}$  is decorrelation from processing errors [10].

### 4. Polarization

The CCD challenge dataset has three different polarization types: a) horizontal-horizontal (HH), b) vertical-vertical (VV), and c) horizontal-vertical (HV). The concept of vertical and horizontal polarization is typically referenced to the antenna orientation with respect to ground [11], as presented in Figures 4, 5, and 6. In addition, the direction of polarization is referenced with respect to the electric field distribution across an antenna. In the context of SAR, the polarization differences correspond to the orthogonality of the antennas. Specifically, two antennas are oriented in such a way to form a 90-degree intersection.

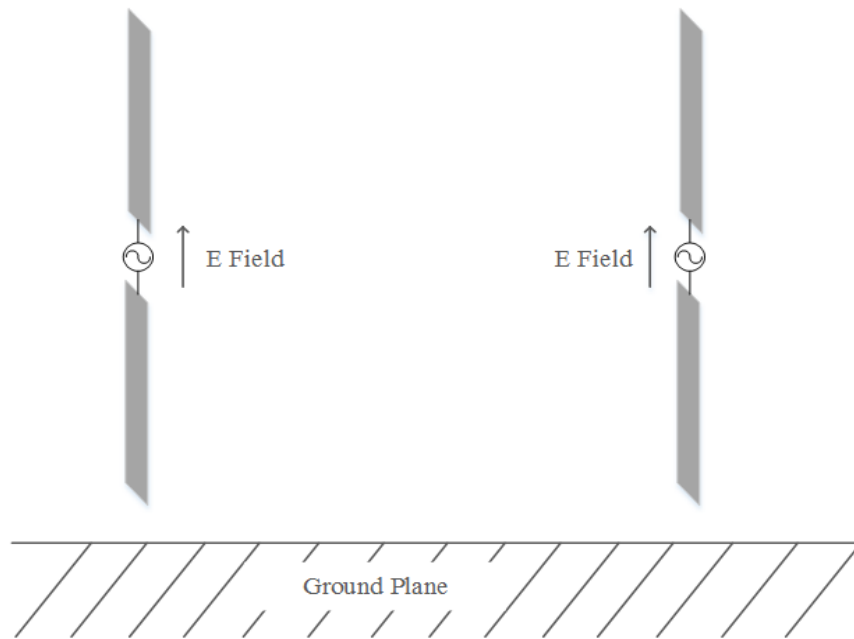


Figure 4. Antennas Oriented in VV Polarization

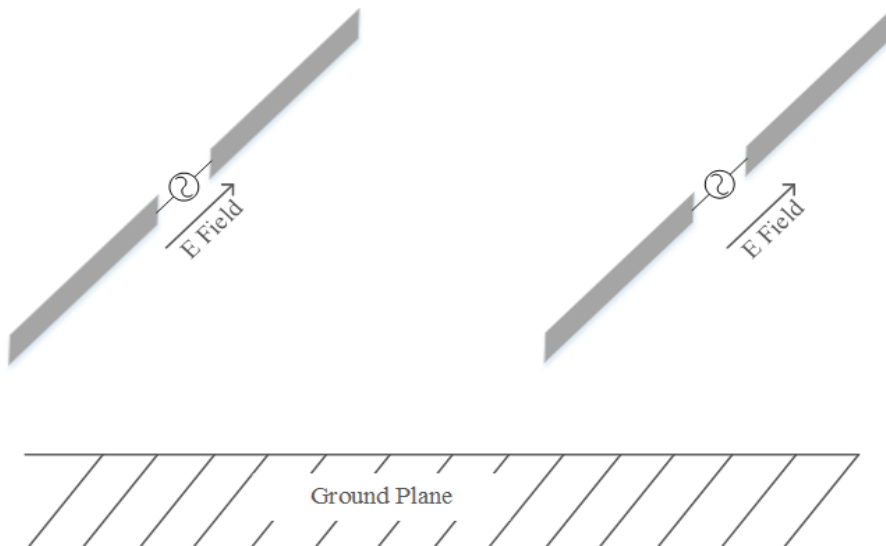


Figure 5. Antennas Oriented in HH Polarization

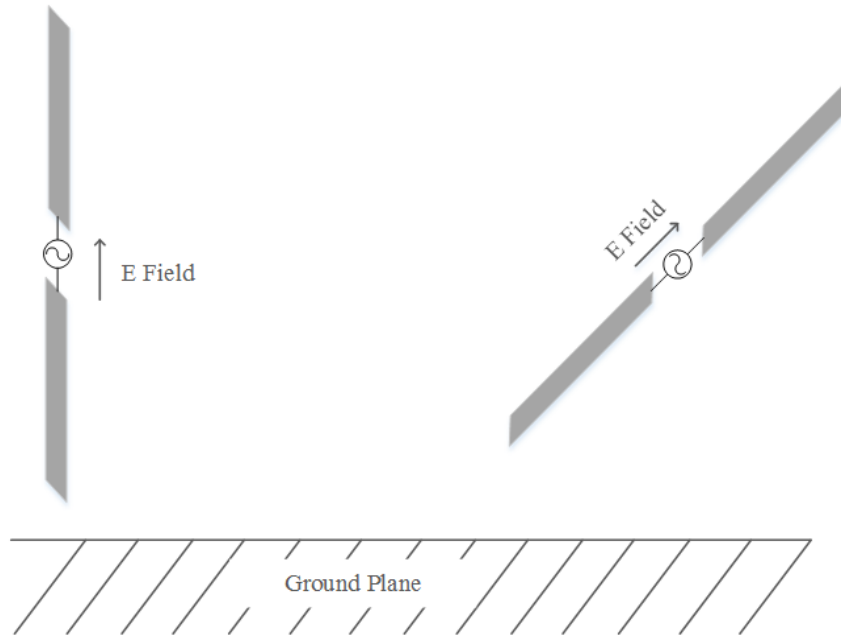


Figure 6. Antennas Orientated in HV Polarization

## 5. Repeat Pass

Repeat passes of the SAR platform are used to generate the metrics for all of the change detection methods which are investigated in this thesis research. Repeat pass corresponds to either the difference between two images taken at two different times or implies that multiple SAR images have been collected at multiple different time intervals. For the current thesis research, only two pass collections were used to evaluate algorithm performance. In the subsequent analysis, there are references to a “mission image” and “reference image.” The mission image is a baseline for comparison of the resulting changes in the reference image. The mission and reference images are seen in Figure 1.

### III. CHANGE DETECTION

In this chapter, we describe the different change detection algorithms that are investigated in this work. All of the change detection algorithms use a moving window, as described in Chapter II Section B.1. In addition, a functional block diagram for the change detection algorithms of Sections A-D is shown in Figure 7. The reference and mission images in this general change detection algorithm functional block diagram are passed through a sliding window to reduce high frequency speckle in the images. The next step is the passing of the data through the change detection method. Finally, the output is passed through a threshold detector to rule if pixels are classified as a valid change.

In Section E, a coherent change detection method, which was presented by Miriam Cha, et al., combined two of the algorithms investigated in the current thesis research and obtained improved change detection results overall compared to the use of the separate algorithms individually [6].

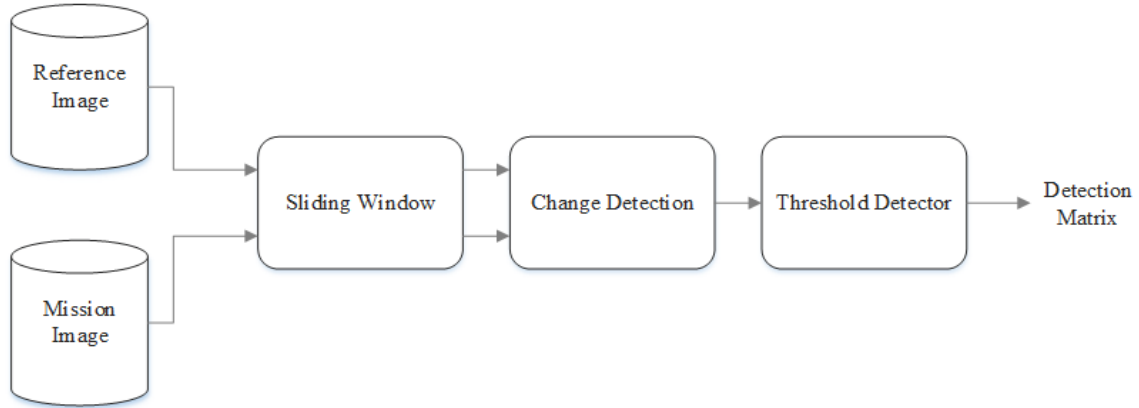


Figure 7. General Change Detection Algorithm Flowchart

### A. INCOHERENT CHANGE DETECTION

The incoherent change detection (ICCD) method is effective and efficient at evaluating large-scale changes in scenes of interest. This calculation is simpler than the other change detection methods discussed herein; however, one of the primary drawbacks of ICCD is that phase information is not retained from the calculation of the relevant ratio change metric. Instead, ICCD uses the mean-square amplitude of a local set of pixels corresponding to two passes in order to determine if change has occurred at each image pixel location. The ratio change metric is defined via

$$R = \frac{\sum_{k=1}^N |f_k|^2}{\sum_{k=1}^N |g_k|^2}, \quad (6)$$

where  $|f_k|^2$  and  $|g_k|^2$  are the mean-square pixel amplitudes of passes  $f$  and  $g$ , respectively, and  $R$  is the ratio change metric. Inspection of Equation (6) reveals that the ratio change metric can have values from zero to infinity. Touzi [5] created a ratio detector defined via

$$r = \begin{cases} R & \text{if } R \leq 1 \\ R^{-1} & \text{if } R > 1 \end{cases}, \quad (7)$$

in order to bound the possible range of values to lie between zero and unity. The variable  $R$  is the ratio change metric in Equation (6), and  $r$  is the modified ratio change metric if  $R$  exceeds unity. The primary purpose of this ratio detector is to avoid complications of having two different thresholds to check for change.

### B. COHERENT CHANGE DETECTION

Coherent change detection is effective at determining small changes in SAR images, e.g., footprints, tire tracks, or tree leaves. The change statistic for CCD ranges from 0 to 1 to show how likely the pixel under test has changed. The change statistic for CCD is

$$\hat{\rho} = \frac{\left| \sum_{k=1}^N f_k^* g_k \right|}{\sqrt{\sum_{k=1}^N |f_k|^2 \sum_{k=1}^N |g_k|^2}}. \quad (8)$$

In Equation (8),  $|f_k|$  is a set of complex pixel data for the mission image,  $|g_k|$  is a set of complex pixel data for the reference image, and  $\hat{\rho}$  is the coherence estimator. The numerator is the complex conjugate product. The denominator is a geometric mean of the images.

### C. ALTERNATIVE COHERENT CHANGE DETECTION

Berger [6] introduced an alternative coherent change detection (ACCD) algorithm which is based upon the use of the arithmetic mean instead of the geometric mean within Equation (6). This algorithm yields superior results in comparison to the CCD method for cases in which the backscatter powers or variances between two passes are equal. This ACCD change statistic is

$$\hat{\rho} = \frac{2 \left| \sum_{k=1}^N f_k^* g_k \right|}{\sum_{k=1}^N |f_k|^2 + \sum_{k=1}^N |g_k|^2} \quad (9)$$

Here, the variable  $f$  represents a set of complex-valued image pixel data for the mission image,  $g$  gives the corresponding data for the reference image, and the denominator represents the arithmetic mean of the clutter power in the two images.

### D. LOG LIKELIHOOD CHANGE STATISTIC

The log-likelihood change statistic (LLCS) detector combines methodologies which are based upon the evaluation of changes in both backscatter power and phase. The LLCS detector has been shown to be superior to ICCD and CCD methods [9]. The full derivation of the LLCS detector is presented in [12], and the final change metric is

$$z = Tr \left\{ \left( Q_0^{-1} - Q_1^{-1} \right) \sum_{k=1}^N \underline{X}_k \underline{X}_k^H \right\}, \quad (10)$$

with  $\underline{X}_k^H$  is the Hermitian transpose of the vector  $\underline{X}$ ,  $z$  is the LLCS change statistic and is expressed in units of dB. In addition,  $\underline{X}_k$  is the  $k^{\text{th}}$  vector containing a local neighborhood of pixels and is shown to be the concatenation of the mission image  $F$  and reference image  $G$  pixel amplitudes:

$$\underline{X} = [\underline{F}, \underline{G}]^T. \quad (11)$$

The  $Q$  matrices are the covariance matrices of the unchanged and changed scenes, respectively,

$$Q_0 = \begin{bmatrix} Q_F & Q_{FG} \\ Q_{FG}^* & Q_{G_0} \end{bmatrix}, \quad (12)$$

and

$$Q_1 = \begin{bmatrix} Q_F & 0 \\ 0 & Q_{G_1} \end{bmatrix}. \quad (13)$$

Here  $Q_F$ ,  $Q_{G_0}$ , and  $Q_{G_1}$  are the mean backscatter powers of the mission image  $F$  and unchanged/changed scenes of reference image  $G$ . In addition,  $Q_{FG}$  is the cross correlation between the images  $F$  and  $G$  and can be represented by

$$Q_{FG} = E\{\underline{F}\underline{G}^H\}. \quad (14)$$

The dataset used in this thesis research contains three different polarizations which can be used in the LLCS detector [13]. Preiss extended the LLCS detector to include all polarizations available from a dataset to enhance the LLCS performance. The  $z$ -test statistic remains the same as in Equation (10), but Equation (11) is modified to

$$\underline{X} = [\underline{F}_1, \underline{F}_2, \underline{F}_3, \underline{G}_1, \underline{G}_2, \underline{G}_3]^T. \quad (15)$$

Here, the subscripts 1, 2, and 3 represent different polarizations. In the context of the dataset for this thesis research, the subscripts represent HH, VV, and HV polarizations, respectively. The matrices in Equations (12) and (13) gives six by six matrices shown as



$$\mathcal{Q}_0 = \begin{bmatrix} \mathcal{Q}_{F_{11}} & \mathcal{Q}_{F_{12}} & \mathcal{Q}_{F_{13}} & \mathcal{Q}_{F_1 G_1} & \mathcal{Q}_{F_1 G_2} & \mathcal{Q}_{F_1 G_3} \\ \mathcal{Q}_{F_{12}}^* & \mathcal{Q}_{F_{22}} & \mathcal{Q}_{F_{23}} & \mathcal{Q}_{F_2 G_1} & \mathcal{Q}_{F_2 G_2} & \mathcal{Q}_{F_2 G_3} \\ \mathcal{Q}_{F_{13}}^* & \mathcal{Q}_{F_{23}}^* & \mathcal{Q}_{F_{33}} & \mathcal{Q}_{F_3 G_1} & \mathcal{Q}_{F_3 G_2} & \mathcal{Q}_{F_3 G_3} \\ \mathcal{Q}_{F_1 G_1}^* & \mathcal{Q}_{F_2 G_1}^* & \mathcal{Q}_{F_3 G_1}^* & \mathcal{Q}_{G_{11}} & \mathcal{Q}_{G_{12}} & \mathcal{Q}_{G_{13}} \\ \mathcal{Q}_{F_1 G_2}^* & \mathcal{Q}_{F_2 G_2}^* & \mathcal{Q}_{F_3 G_2}^* & \mathcal{Q}_{G_{12}}^* & \mathcal{Q}_{G_{22}} & \mathcal{Q}_{G_{23}} \\ \mathcal{Q}_{F_1 G_3}^* & \mathcal{Q}_{F_2 G_3}^* & \mathcal{Q}_{F_3 G_3}^* & \mathcal{Q}_{G_{13}}^* & \mathcal{Q}_{G_{23}}^* & \mathcal{Q}_{G_{33}} \end{bmatrix}, \quad (16)$$

and

$$\mathcal{Q}_1 = \begin{bmatrix} \mathcal{Q}_{F_{11}} & 0 & 0 & 0 & 0 & 0 \\ 0 & \mathcal{Q}_{F_{22}} & 0 & 0 & 0 & 0 \\ 0 & 0 & \mathcal{Q}_{F_{33}} & 0 & 0 & 0 \\ 0 & 0 & 0 & \mathcal{Q}_{G_{11}} & 0 & 0 \\ 0 & 0 & 0 & 0 & \mathcal{Q}_{G_{22}} & 0 \\ 0 & 0 & 0 & 0 & 0 & \mathcal{Q}_{G_{33}} \end{bmatrix}. \quad (17)$$

## E. TWO-STAGE COHERENT CHANGE DETECTION

The two-stage filter combines the concepts of incoherent change detection and coherent change detection [6]. This method has an ICCD stage and an ACCD stage in parallel. The registered changes from each block are passed into a combiner and outputs a change mask. The flowchart in Figure 8 illustrates the process. The image pixels are passed into the ICCD detector. If the backscatter powers are not equal, then it is registered as a change. If the backscatter powers are equal, then the sample coherence is evaluated in the ACCD detector to see if a small-scale change occurred. Any regions remaining are ruled as no change present.

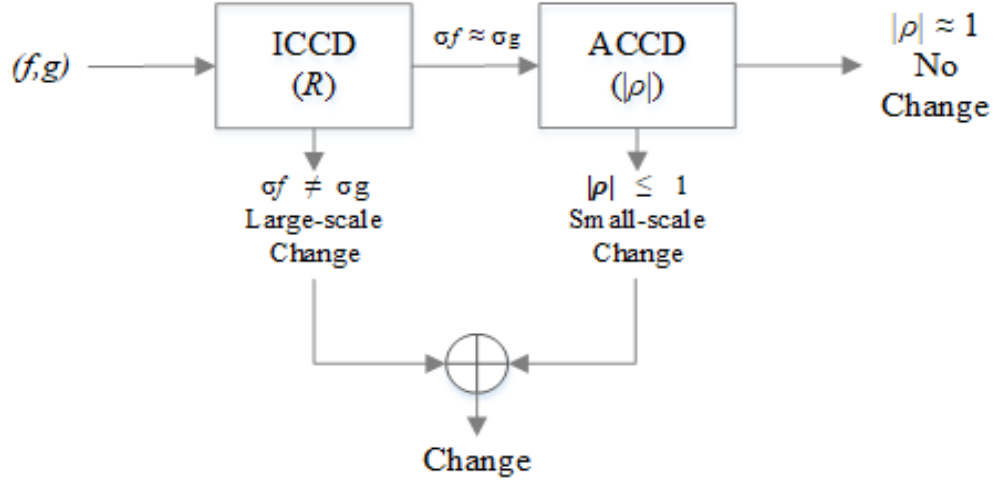


Figure 8. Two-Stage Change Detection Flowchart. Adapted from [6].

The dichotomies of the first and second stage outputs, as shown in Figure 9, are presented in Cha's paper. The figure is a two-dimensional presentation of the regions of validity for the  $H_0$  and  $H_1$  hypotheses. The  $H_0$  hypothesis implies that no change is present, and the  $H_1$  hypothesis implies that change is present. The colored regions are sized based on the thresholds chosen for the ICCD and the ACCD stage. The purple region represents the  $H_1$  hypothesis of change, and the blue region represents the  $H_0$  hypothesis of no change. The variable  $R$  represents the ratio of backscatter powers ratio, and  $|\rho_a|$  is the absolute ACCD coherence value.

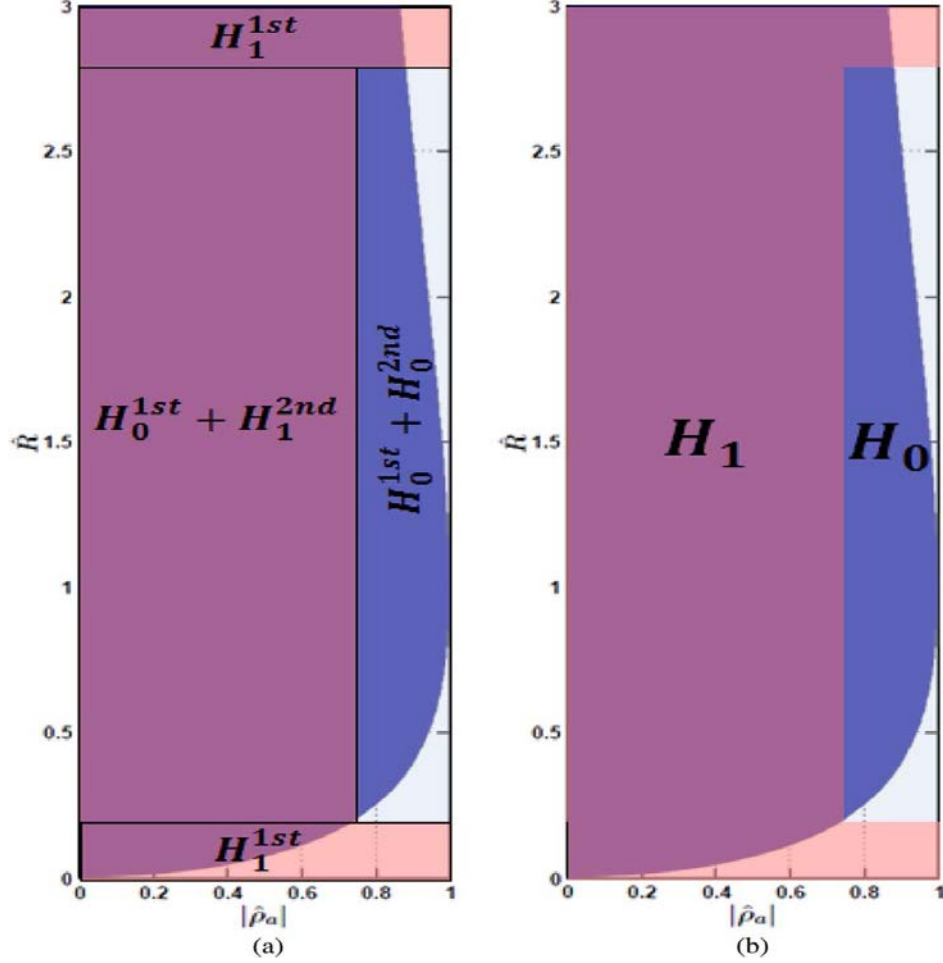


Figure 9. Probability Space of  $H_0$  and  $H_1$  Hypotheses for Two-Stage Change Detection. Source: [6].

The two-stage algorithm incorporates a null hypothesis test on the estimated backscatter ratio. This was shown to decrease the number of false alarms by rejecting pixel intensities that support the hypothesis. The estimated backscatter power  $\hat{R}$  here does not use the Touzi method described in Chapter III Section A. The two-stage method incorporates an  $F$ -test. This test determines if two random variables' variances are the same or different. For the case of the same variance this is called the null hypothesis and for different variance is called the alternative hypothesis. To determine which hypothesis is true, bounds called critical values are found as

$$R_{u,\alpha} = F^{-1}\left(1 - \frac{\alpha}{2}, 2N, 2N\right), \quad (18)$$

and

$$R_{l,\alpha} = F^{-1}\left(\frac{\alpha}{2}, 2N, 2N\right). \quad (19)$$

Here,  $\alpha$  is the significance level, usually 0.05 or 0.01,  $N$  is the number of pixels in a local neighborhood,  $R_{l,\alpha}$  and  $R_{u,\alpha}$  is the lower bound and upper bound of the null hypothesis test, respectively, and  $F^{-1}$  is the  $F$  distribution inverse. Taking an estimated ratio change value, it is compared to the bound values,  $R < R_{l,\alpha}$  or  $R > R_{u,\alpha}$ , which result in change being detected for the ICCD portion of the two-stage method.

## IV. THREE-STAGE CHANGE DETECTION

The two-stage change detection algorithm is improved by combining its output with an extended polarimetric LLCS filter with segmentation. A  $k$ -means clustering algorithm is used for segmentation and is described in Section A. The benefit of using the extended polarimetric LLCS filter is discussed in Section B. The binary operation is discussed in Section C.

The three-stage flowchart is shown in Figure 10. The left path of this flowchart is the combination of segmentation and LLCS filter with the three polarizations complex-datasets. The right path is the same filter as described in Chapter III Section E.

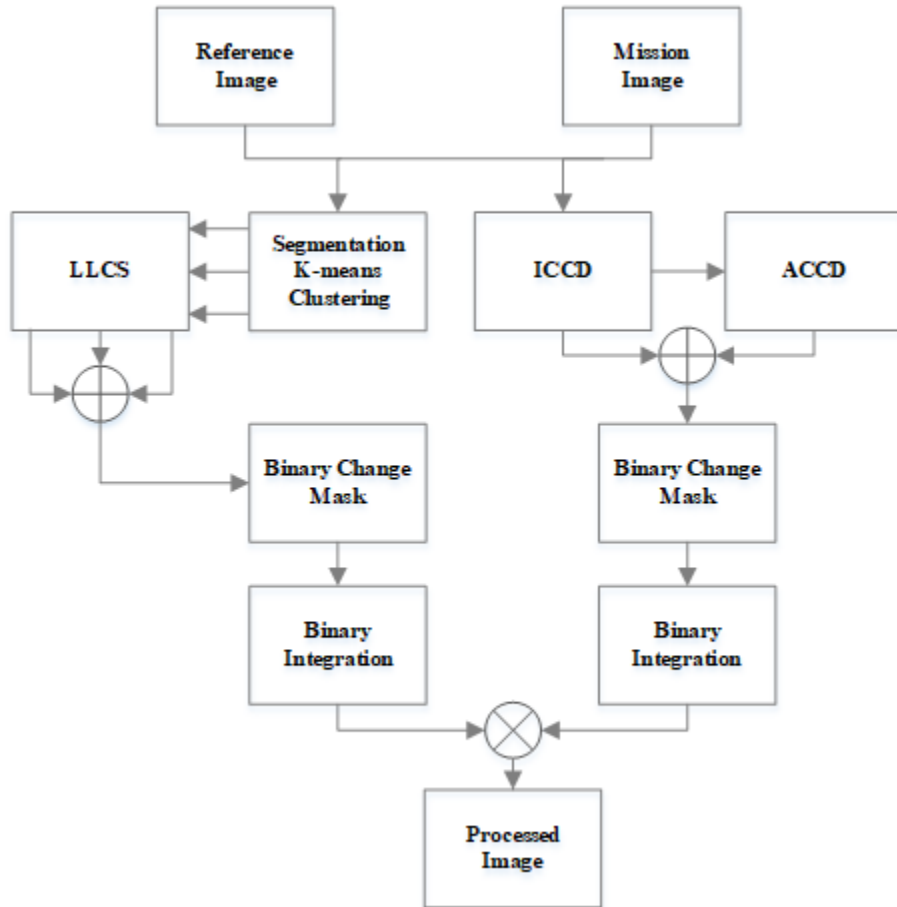


Figure 10. Three-Stage Change Detection Flowchart

## A. K-MEANS CLUSTERING

*K*-means clustering is an algorithm that partitions data into separate regions that share similar means. To find the means, the algorithm identifies data points closest to a centroid and associates those data points to group number, creating multiple clusters of data points.

To illustrate the *k*-means algorithm, a random clustered dataset is presented in Figure 11. The left subfigure represents the random dataset. The right subfigure is the output of the *k*-means algorithm. The three different colors represents which cluster those points belong to and the  $\times$  represent centroid locations. The mathematics laboratory software (MATLAB) built-in function for *k*-means was used in this example.

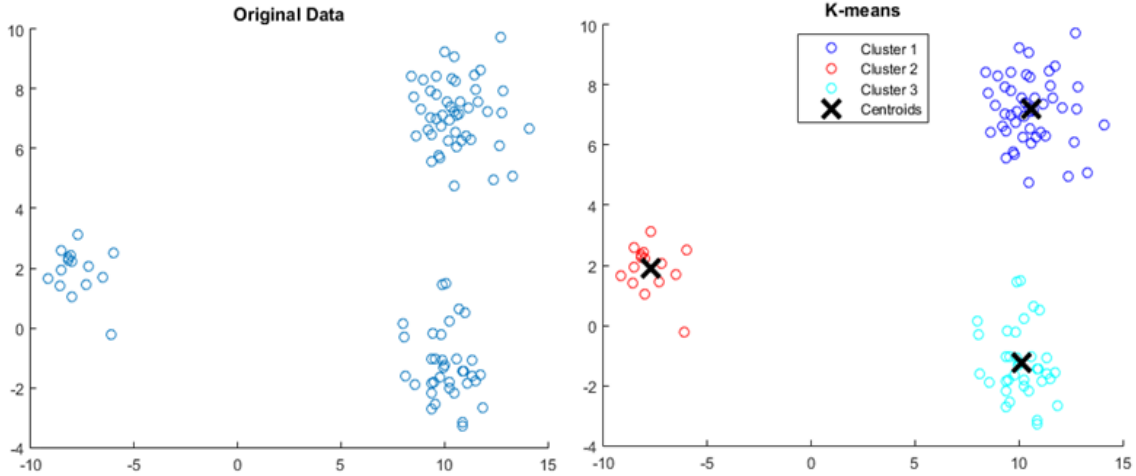


Figure 11. Application of *K*-Means Algorithm

The appropriate name for the MATLAB algorithm is *k*-means++ algorithm. In [14], the authors improved the efficiency of the original *k*-means algorithm and coined the name *k*-means++. The general algorithm is performed in multiple steps. The first step is to select a data point at random and declare this as centroid 1. The second step is to compute the geometric distances from centroid 1 to other data points in the set. The third step is to find the centroid 2 based on the information obtained in step 2. This process is

repeated for the number of steps to achieve a certain probability  $p$  between the clusters. The probability function is

$$p = \frac{D(x)^2}{\sum_{x \in X} D(x)^2}, \quad (20)$$

where  $p$  is the probability of the current data point being a part of a cluster dataset,  $x$  is the sample position, and  $D$  is the distance between  $x$  data points to the current centroid.

The application of the  $k$ -means algorithm to SAR images separates different regions of an image into clusters. The different centroid regions represent objects (buildings/cars), trees or foliage, and shadows. The CCD challenge dataset with  $k$ -means applied is seen in Figure 12. Each of the subfigures in Figure 12 represent a different centroid cluster of the CCD challenge dataset and all were normalized to the maximum amplitude of their respective clusters.

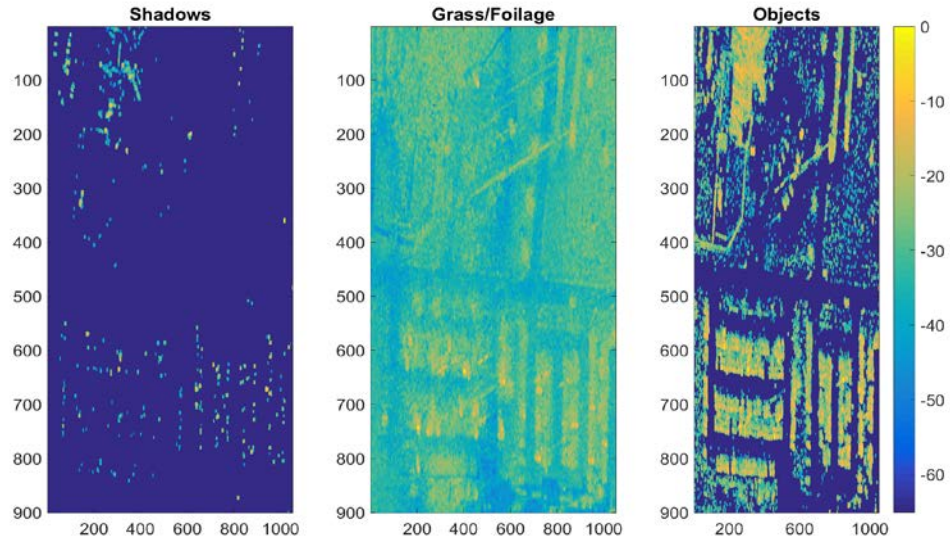


Figure 12. CCD Challenge Problem Dataset with  $K$ -Means Application

## B. EXTENDED LLCS FILTER

The extended LLCS filter incorporates all three polarizations of the CCD challenge problem dataset. The additional polarimetric data is said to improve the false

alarm rate and enhance scene details in [12] and [13]. The use of additional polarizations acts as a speckle decorrelator in the changed scene.

There are two different estimation approaches in [12] using the  $Q$  matrices defined in Equations (12) and (13). The first method is to create or derive a ground truth for the changed areas of the scene. Estimates of  $Q_F$  and  $Q_G$  can be found using Equation (4). Furthermore,  $Q_{FG}$  can be found by the product of Equation (8) and  $\sqrt{Q_F Q_{G_0}}$ , or  $\sqrt{Q_F Q_{G_1}}$ .

The second method of estimating the  $Q$  matrices is to set  $Q_{G_0} = Q_{G_1}$  and calculate  $Q_F$  and  $Q_{G_0}$  using Equation (4). This method diverges from the first because the assumption is the mean backscatter power between the two scenes is approximately equal. This method requires a good estimate of the coherence to be effective.

The extended LLCS filter uses the first method of estimating the  $Q$  matrices with a slight difference. Once the repeat-pass images are segmented, the  $Q$  matrices estimates are generated for the number of classes used in the  $k$ -means algorithm. Then the LLCS change detection is applied to each of the segments and recombined to form the  $z$ -change metric in Equation (10). A flowchart of this process is shown in Figure 13. In this flowchart,  $D$  and  $H$  represent the rows and columns of the scene,  $P$  is the number of polarizations,  $S$  is the number of clusters for the  $k$ -means clustering, and  $W$  represents  $F$  or  $G$  pixel samples.

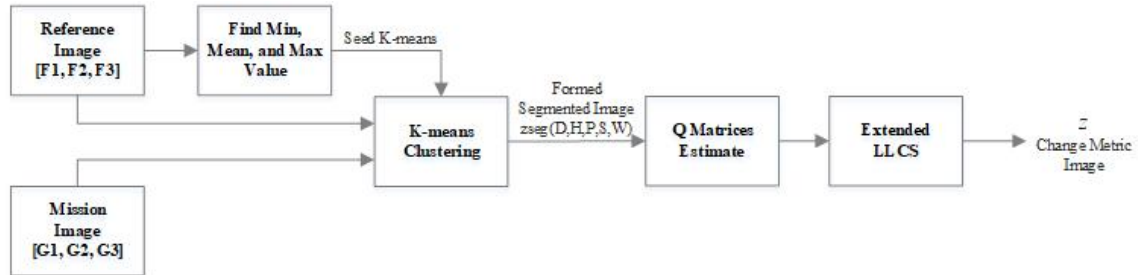


Figure 13. Extended LLCS and Segmentation Process Flowchart



## C. BINARY OPERATIONS

The two binary operations used in the three-stage algorithm are binary thresholding and binary integration [15]. Binary thresholding is used to convert change data to either a 1 or a 0 to represent change or no change, respectively. This is done to only show the changed regions of interest.

Binary integration is the step after the binary change mask to help “round-out” changes in the image. Furthermore, binary integration aids in the reduction of false alarms caused by speckle in the dataset.

### 1. Binary Thresholding

To determine if a change is made the following conditions are used

$$C = (x \geq T) , \quad (21)$$

or

$$C = (x < T) , \quad (22)$$

and,

$$C \in \{0,1\} , \quad (23)$$

where  $C$  is binary for change or no change,  $x$  is a two-stage filtered pixel amplitude, and  $T$  is the threshold to rule change or no change.

### 2. Binary Integration

The binary integrator uses a sliding window to sweep across the binary threshold matrix output from Equations (21), (22), and (23). For each of the local sliding neighborhoods, the sum is compared to a threshold to decide if it was a change or a false alarm due to speckle. The binary integrator is defined by

$$P(m) = \sum_k^N C(k) \geq U \quad (24)$$

or

$$P(m) = \sum_k^N C(k) < U , \quad (25)$$

and

$$P(m) \in \{0,1\}, \quad (26)$$

where  $P(m)$  is the change identifier of the  $m$  pixel,  $C$  is the change matrix from the binary threshold,  $k$  is index of the current pixel,  $N$  is the total number of pixels in the local neighborhood, and  $U$  is the threshold.

An example is presented in Figure 14 to show a binary integrator application. The black dots represent pixels identified as change, and the white dots are no change. Binary integration is applied to the neighborhood of pixels in the left subfigure, and the right subfigure presents the result. The threshold  $U$  is equal to four pixels, and  $N$  is equal to nine.

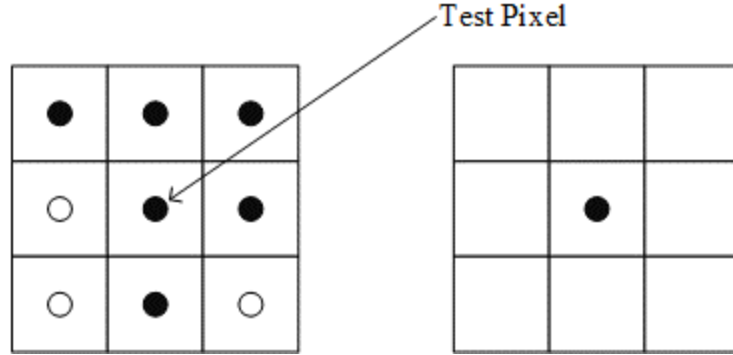


Figure 14. Binary Integrator Neighborhood Example

To show the effect of binary operations, both were applied to the two-stage filter output of the CCD challenge dataset. The union of the two-stage filter with the binary operations is the right path in Figure 10. The binary operations have a visual impact in the number of false alarms seen in Figure 15. The  $U$  threshold and number of pixels  $N$  had to be found by trial and error for best performance. For Figure 15, the threshold  $U$  and number of pixels  $N$  were 10 and 25, respectively. Change is represented by the yellow pixels and no change is represented as blue pixels. A large concentration of false alarms is shown in the red rectangle in the pre-binary integrator output.

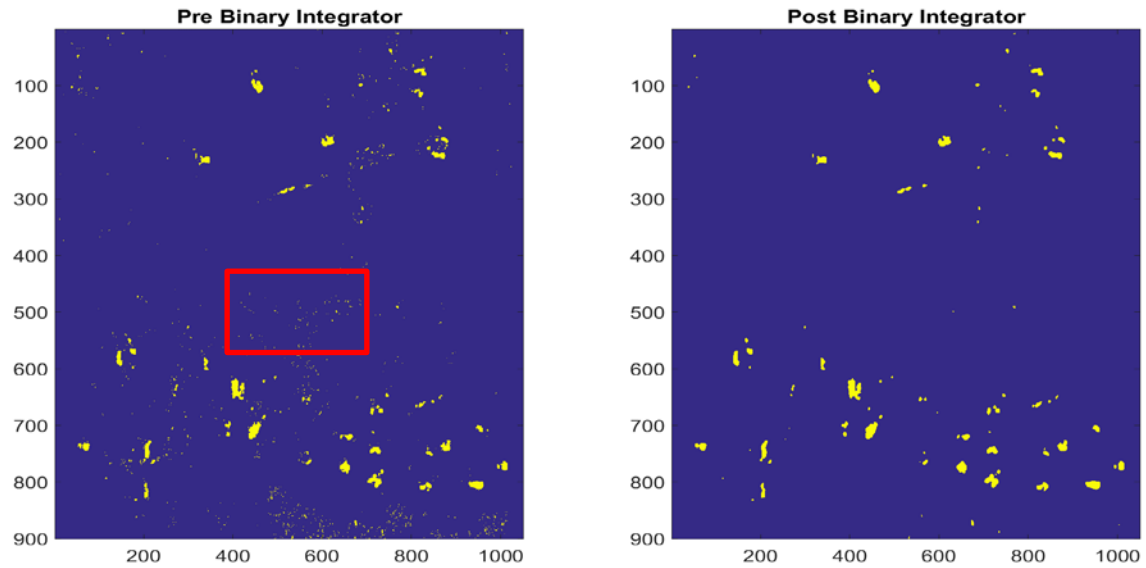


Figure 15. Pre- and Post-binary Integrator Images

The red rectangle was enhanced and compared to the post binary integration operation in Figure 16 to see the effect of the binary operations clearly.

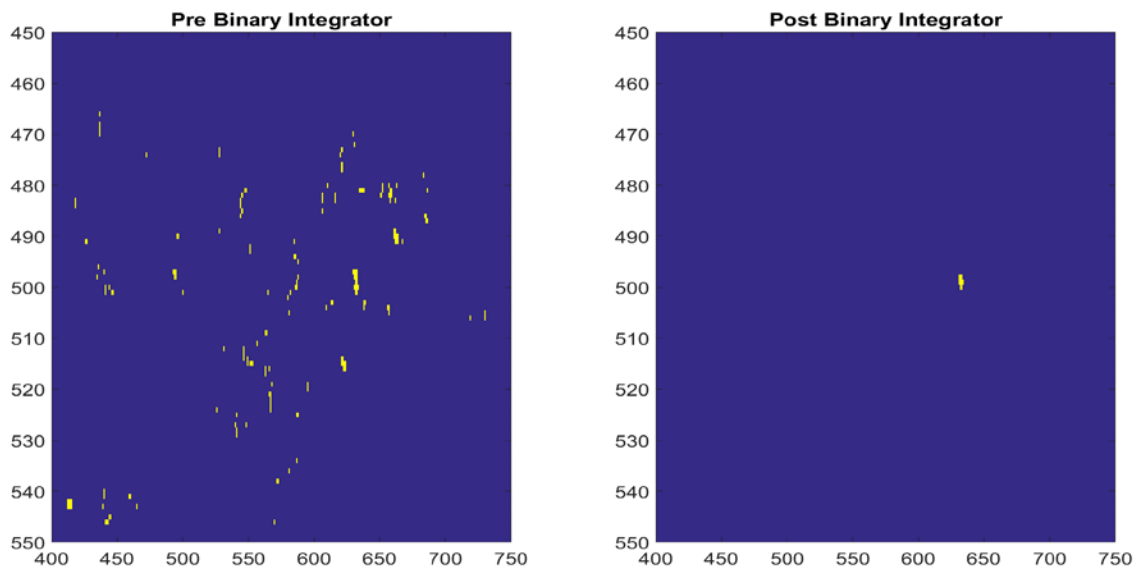


Figure 16. Focused Red Area of Figure 15

THIS PAGE INTENTIONALLY LEFT BLANK

## V. CHANGE DETECTION SIMULATION RESULTS

In this chapter, three of the change detection methods are investigated using a basic simulator. The three methods are ICCD, CCD, and LLCS. Simulator design and general simulator parameters are discussed in Section A, and the simulator results for the change detection methods are discussed in Section B.

### A. SIMULATOR MODEL AND PARAMETERS

The simulator consists of two image generators, a change detection method, a simple threshold detector, and a mean estimator for the probabilities. The two image generators generate Gaussian-noise images. One image has unity variance and zero mean, while the other is altered for a specific test event. The two images are passed into the change detection algorithm, and a result image is generated by comparing the change metric to a threshold  $\tau$ . This is repeated for the number of trials  $V$  for each value of  $\tau$ . Based on the number of change metrics  $\sigma$  being tested, the simulator executes  $V\tau_{length}\sigma_{length}$  times. The flowchart for the simulator is shown in Figure 17.

The simulator starts by generating Gaussian pairs with chosen mean and covariance properties. These test images are passed into the change detection algorithm under test. The change metric output is compared against a simple threshold detector. Finally, the mean probability of detection is calculated for the number of trials for a set threshold.

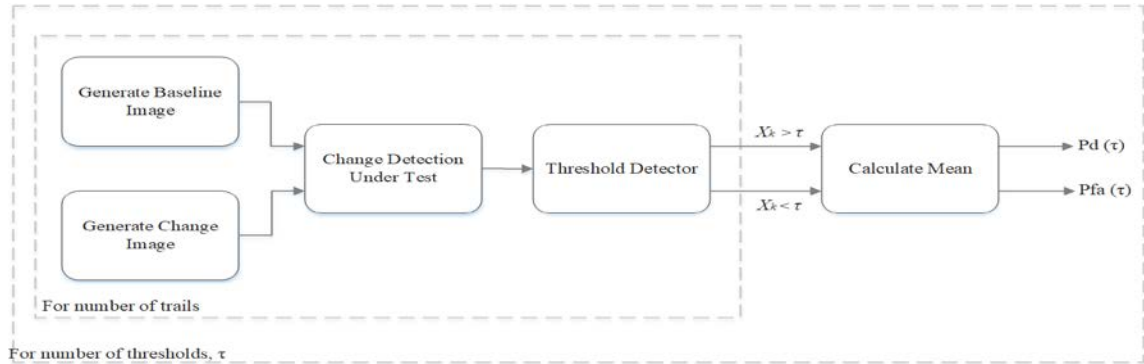


Figure 17. Change Detection Simulator Flowchart

The test images are Gaussian bivariate random vectors with zero mean and covariance matrix  $Q$ . They each have a length of 1024 samples. For the simulations of the CCD and LLCS methods, correlation needs to be introduced between the two images. To create correlated vectors with specified variances, the following is used

$$\underline{Z} = [\underline{X}, \underline{Y}]^T Q, \quad (27)$$

where  $\underline{X}$  and  $\underline{Y}$  are the Gaussian bivariate random vectors,  $Q$  is the covariance matrix in Equation (12), and  $\underline{Z}$  is the transformed pair of Gaussian bivariate random vectors. The Gaussian vectors are reshaped to a 32 by 32 image after transformation.

The simulator is a basic Monte Carlo simulator with Gaussian inputs. In order to achieve repeatable results, a minimum number of trials must be used. The number of required trials is estimated by

$$M \geq \frac{[A^{-1}(\alpha/2)]^2 (1-P)}{\varepsilon^2 P}, \quad (28)$$

where  $A^{-1}(\alpha/2)$  is the complementary cumulative distribution function inverse,  $\alpha$  is the significance level,  $P$  is the a priori probability of detection, and  $\varepsilon$  is the error tolerance [16]. The minimum number of required trials is found to be 2,177, using  $\alpha = 0.05$ ,  $P = 0.9$ , and  $\varepsilon = 0.01$  (1%). For the simulator, the number of trials is chosen to be 2500 to further reduce error.

Only three of the six change detection methods are simulated in this paper: ICCD, CCD, and LLCS. These three are viewed as the base algorithms for change detection. The other three change detection methods are composites of these three base methods.

The primary goal of creating the simulator is to ensure the change detection algorithms are similar to Preiss's findings in [9]. The results' figures have theoretical curves created by the probability density functions (pdf) listed in Preiss's paper. For full derivations for the pdfs refer to [9], [12], [13].

## B. SIMULATOR RESULTS

The ICCD ROC curve is shown in Figure 18. The solid lines are the theoretical ICCD results using backscatter powers of 1, 3, 5, and 10 dB. The dotted lines give the corresponding simulated results. The theoretical curves are generated by the pdf

$$p(\hat{r} | R) = \frac{\Gamma(2N)}{\Gamma(N)^2} \left( \frac{R^N}{(\hat{r} + R)^{2N}} + \frac{R^{-N}}{(\hat{r} + R^{-1})^{2N}} \right) \hat{r}^{N-1}. \quad (29)$$

wherein  $\Gamma(\cdot)$  is the gamma function,  $N$  is the number of pixels in the local neighborhood,  $R$  is the true backscatter ratio, and  $\hat{r}$  is the estimated backscatter ratio. Numerical integration was performed on Equation (29) to find the probability of detection ( $P_d$ ) and probability of false alarm ( $P_{fa}$ ).

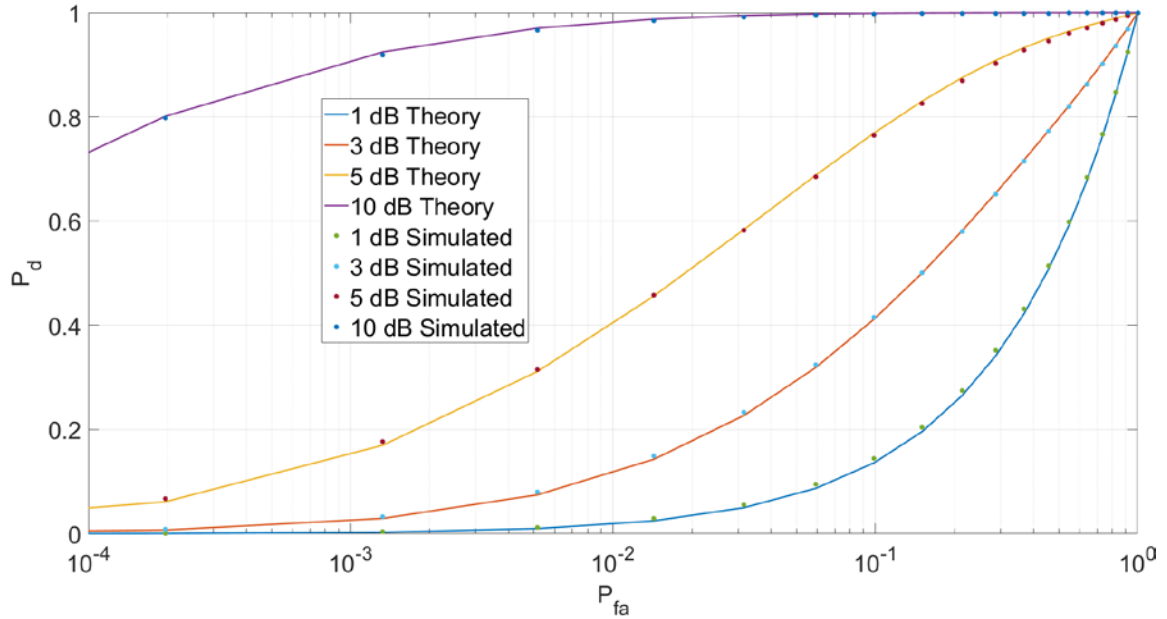


Figure 18. ICCD Simulated versus Theoretical Results

The ICCD is a measure of the ratio of the backscatter powers of two images, whereas the CCD is a measure of coherence between two images. The change metric for the CCD algorithm is coherence. The theoretical pdf as a function of coherence is described as

$$p(\theta | \gamma, N) = 2(N-1)(1-\gamma^2)^N \theta(1-\theta^2)^{(N-2)} {}_2G_1(N, N; 1; \gamma^2 \theta^2), \quad (30)$$

where  $\gamma$  represents true coherence value,  $\theta$  is the estimated coherence value,  $N$  is the number of local neighborhood pixels, and  ${}_2G_1(\cdot)$  is the Gauss hypergeometric function. The pdf is numerically integrated to give the theoretical curves in Figure 19.

The change metric values for CCD are 0.45, 0.6, 0.75, and 0.9. These values are dimensionless but represent the coherence between the baseline and change image. The CCD method starts to perform reasonably well once coherence is above 0.62. For a coherence value of 0.9, the CCD method achieved above a  $P_d$  of 0.9 and  $P_{fa}$  of  $10^{-4}$ . The CCD ROC curve is shown in Figure 19. The solid lines are the theoretical CCD results using backscatter powers of 0.45, 0.6, 0.75, and 0.9. The dotted lines give the corresponding simulated results.

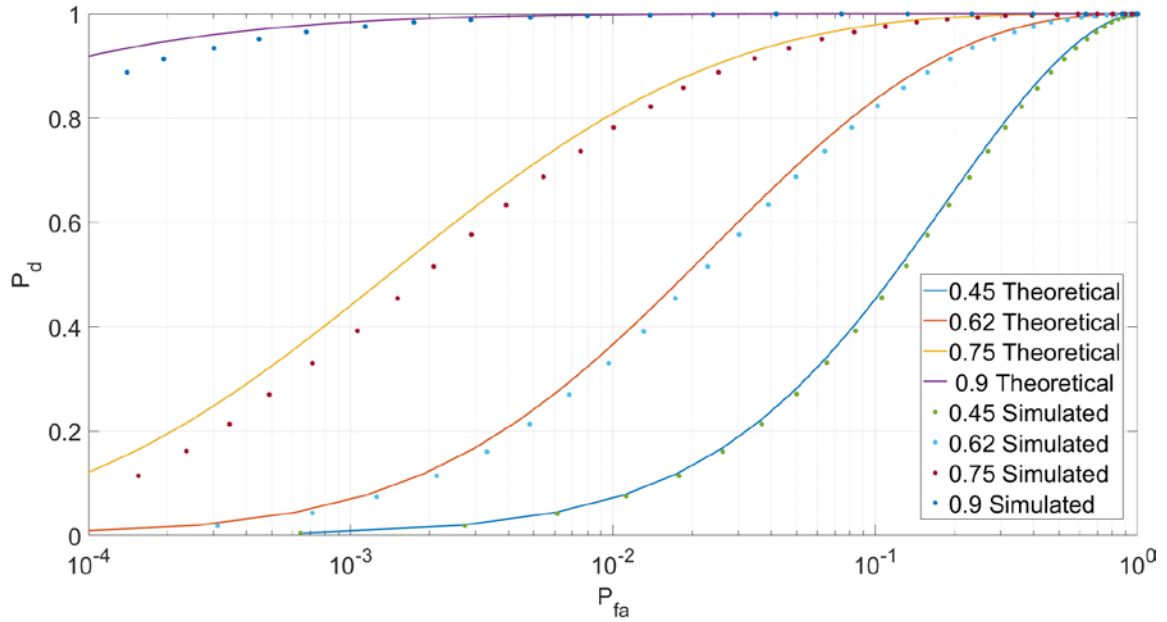


Figure 19. CCD Simulated versus Theoretical Results

The LLCS detector estimates the coherence and the mean backscatter ratio of two images. To verify the LLCS algorithm performance, two separate simulations were performed. One simulation keeps the coherence static while the mean backscatter power



ratio is varied. The second is the opposite case with static backscatter power and varied coherence.

The coherence portion of LLCS was simulated first and shows better performance than the CCD algorithm. For a coherence value of 0.62 and a  $P_{fa}$  of  $10^{-4}$ , the  $P_d$  is 0.48. In comparison, the CCD algorithm with a coherence of 0.62 has a  $P_d$  of 0.006. The LLCS shows two orders of magnitude improvement. The ROC curves for varying the coherence of the LLCS are seen in Figure 20. The solid lines are the theoretical results using coherence values of 0.45, 0.6, 0.75, and 0.9. The dotted lines represent the corresponding simulated results. The variance of the test images were set to unity.

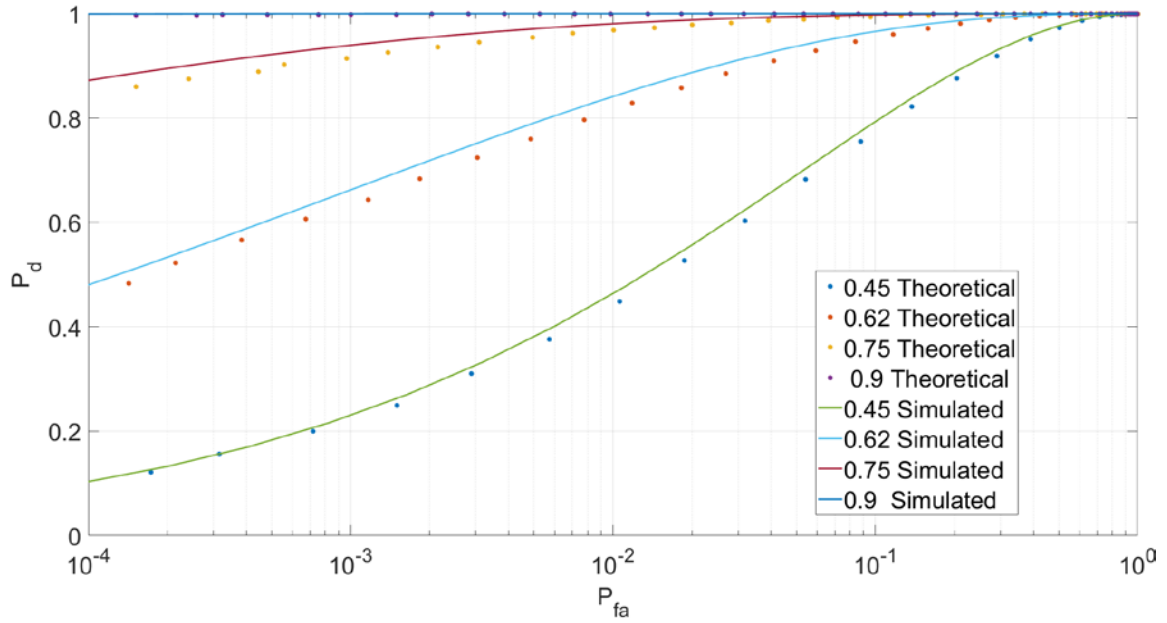


Figure 20. Simulated Constant Power LLCS versus Theoretical Results

The theoretical curves in Figure 20 were created for  $z \leq 0$

$$p(z) = \frac{\exp\left(\frac{z}{\lambda_1 C_{11}}\right)}{\Gamma^2(N)(\lambda_1 C_{11} \lambda_2 C_{22})^N} \sum_{p=0}^{N-1} \left[ \binom{N-1}{p} \frac{\Gamma(2N-p-1)}{v^{2N-p-1}} (-z)^p \right], \quad (31)$$

and for  $z > 0$

$$p(z) = \frac{\exp\left(\frac{-z}{\lambda_2 C_{22}}\right)}{\Gamma^2(N)(\lambda_1 C_{11} \lambda_2 C_{22})^N} \sum_{p=0}^{N-1} \left[ \binom{N-1}{p} \frac{\Gamma(2N-p-1)}{v^{2N-p-1}} z^p \right]. \quad (32)$$

Here,  $z$  is the change metric,  $\lambda_n$  are the eigenvalues for the  $Q$  matrices defined in Equations (12) and (13),  $C$  is the transformed covariance values,  $N$  is the total neighborhood pixels, and  $v$  is defined as

$$v = \frac{1}{\alpha} + \frac{1}{\beta}, \quad (33)$$

where

$$\alpha = \lambda_1 C_{11} (1 - \rho^2), \quad (34)$$

and

$$\beta = \lambda_2 C_{22} (1 - \rho^2). \quad (35)$$

Here,  $\rho$  represents true coherence of the image.

The LLCS simulation using constant coherence yields better performance than the ICCD method. For a mean backscatter power of 5 dB and  $P_{fa}$  of  $10^{-4}$ , the ICCD has a  $P_d$  of 0.04. In comparison, the LLCS achieves a  $P_d$  of 0.97. The LLCS equal coherence results can be seen in Figure 21. The solid lines are the theoretical results using backscatter powers of 0, 1, 3, 5, and 10 dB. The dotted lines represent the corresponding simulated results. A constant value of 0.62 was used for the coherence.

The theoretical curves are defined for  $z \leq 0$

$$p(z) = \frac{(1 - \rho^2)^N e^{\left(\frac{z}{\alpha}\right)}}{\Gamma(N)(\alpha\beta)^N} \sum_{k=0}^{\infty} \left[ \mu_k \sum_{p=0}^{N+k-1} \left[ \binom{N+k-1}{p} \frac{\Gamma(2k+2N-p-1)}{v^{2k+2N-p-1}} (-z)^p \right] \right], \quad (36)$$

and for  $z \leq 0$ ,

$$p(z) = \frac{(1 - \rho^2)^N e^{\left(\frac{-z}{\beta}\right)}}{\Gamma(N)(\alpha\beta)^N} \sum_{k=0}^{\infty} \left[ \mu_k \sum_{p=0}^{N+k-1} \left[ \binom{N+k-1}{p} \frac{\Gamma(2k+2N-p-1)}{v^{2k+2N-p-1}} (-z)^p \right] \right], \quad (37)$$

wherein,  $\rho$  is the true coherence of the scene,  $N$  is the number of local pixels under test,  $v$  is defined in Equation (33),  $\alpha$  is defined in Equation (34),  $\beta$  is defined in Equation (35), and  $\mu_k$  is defined as

$$\mu_k = \frac{1}{\Gamma(N+k)k!} \left( \frac{\rho^2}{\alpha\beta} \right)^k. \quad (38)$$

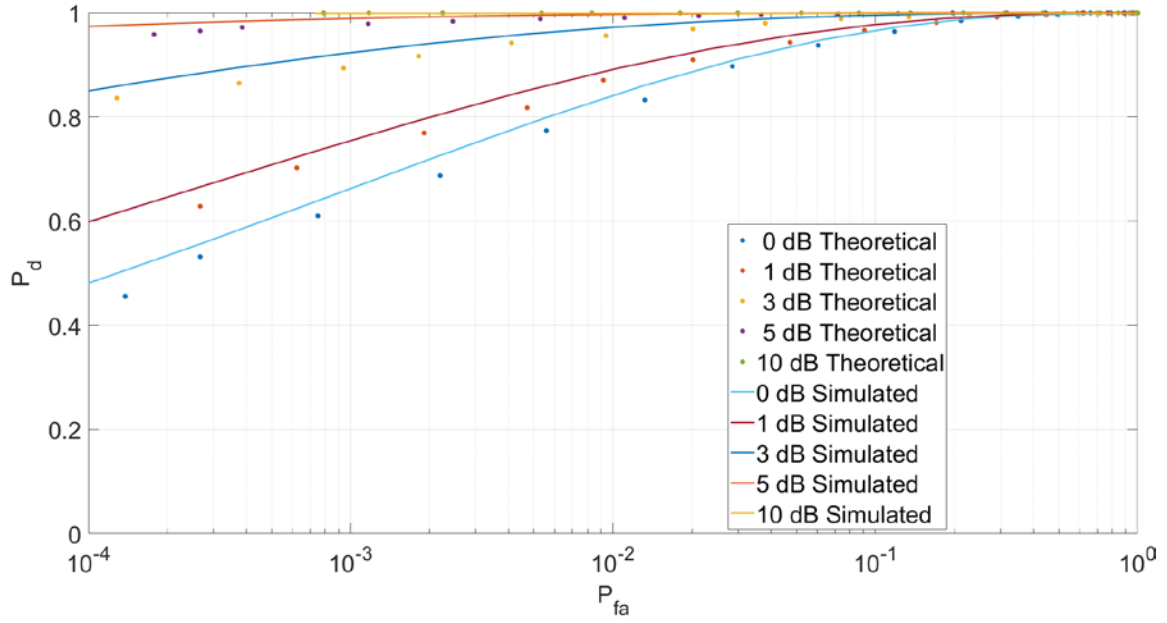


Figure 21. Simulated Constant Coherence LLCS versus Theoretical Results

THIS PAGE INTENTIONALLY LEFT BLANK

## VI. CHANGE DETECTOR INVESTIGATION

The CCD Challenge Problem dataset was collected by an AFRL airborne X-band SAR sensor. There are ten repeat passes of the same geographic scene captured on the same day. The images contain foliage, buildings, and vehicles. Parameters for the airborne sensor are presented in Table 1.

Table 1. AFRL SAR Sensor Parameters. Adapted from [8].

<b>Center Frequency</b>	9.6 GHz
<b>Bandwidth</b>	640 MHz
<b>Polarizations</b>	HH, VV, and HV
<b>Image Sampling Spacing (<math>\Delta s</math>)</b>	0.2 m
<b>Image Pixel Dimensions</b>	4501 pixels by 4501 Pixels
<b>Depression Angle</b>	45 degrees
<b>Image Data Type</b>	Complex, 32 bit floating point
<b>CCD Challenge Data Files</b>	Reference: FP0121 Mission: FP0124

In this chapter, there are comparative assessments of the image changes to common objects e.g., cars, roads, running tracks, etc. In order to relate suspected changes to objects, a conversion between pixel and meters is found from

$$L = \Delta l / \Delta s, \quad (39)$$

where  $\Delta l$  is the number of pixels in a given region of interest,  $\Delta s$  is the image sampling spacing from Table 1, and  $L$  is the length in meters. The average dimensions of common objects are in Table 2.

Table 2. Average Object Dimensions. Adapted from [17], [18].

<b>Average American Mid-Size Sedan [Length, Width]</b>	[2.66 m, 1.81 m]
<b>Large SUV [Length, Width]</b>	[2.79 m, 1.99 m]
<b>American Highway Lane Width</b>	3.6 m
<b>Running Track Width (One Lane)</b>	1.22 m

## A. DESCRIPTION OF THE AREA OF INTEREST

A subarea was selected from the CCD challenge dataset to use as the area of interest for this investigation. The region has part of what appears to be a cul-de-sac, a large parking lot with cars, a building, a circular track to the left of the building, and other foliage and is shown in Figure 22. One of the horizontal rows in the parking lot is approximately 300 pixels wide. Using Equation (39), we found the length to be 60 m, or approximately 22 cars wide. Assuming the parking lot has two by N spots, there are a total number of 44 potential cars. This allows for many targets of opportunity as well as errors in estimation of the ground truth.

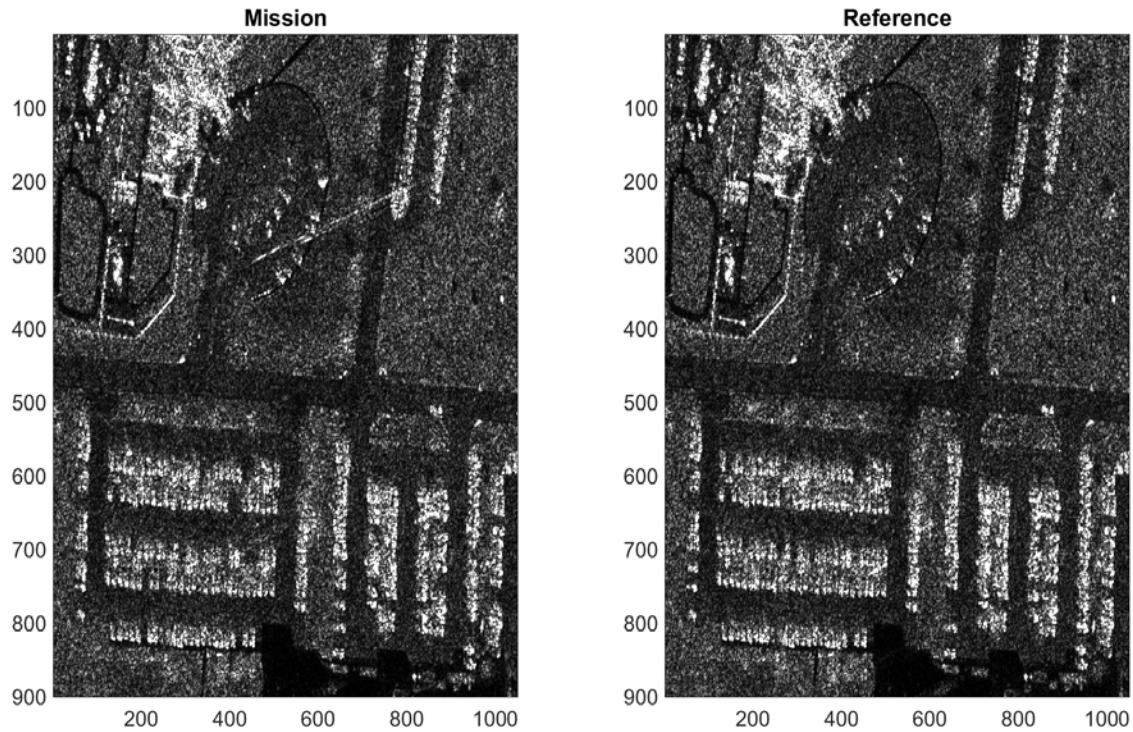


Figure 22. Mission and Reference Images of Area of Interest

## B. GROUND TRUTH

The CCD challenge dataset does not include ground truth data. To generate the ground truth image, both images are overlaid and changes are found visually. The ground truth image is shown in Figure 23 with the mission image for comparison. The black

represents change and white represents no change. There may be more changes possible in the scene, but the 26 boxes identified are sufficient to characterize the change detection methods.

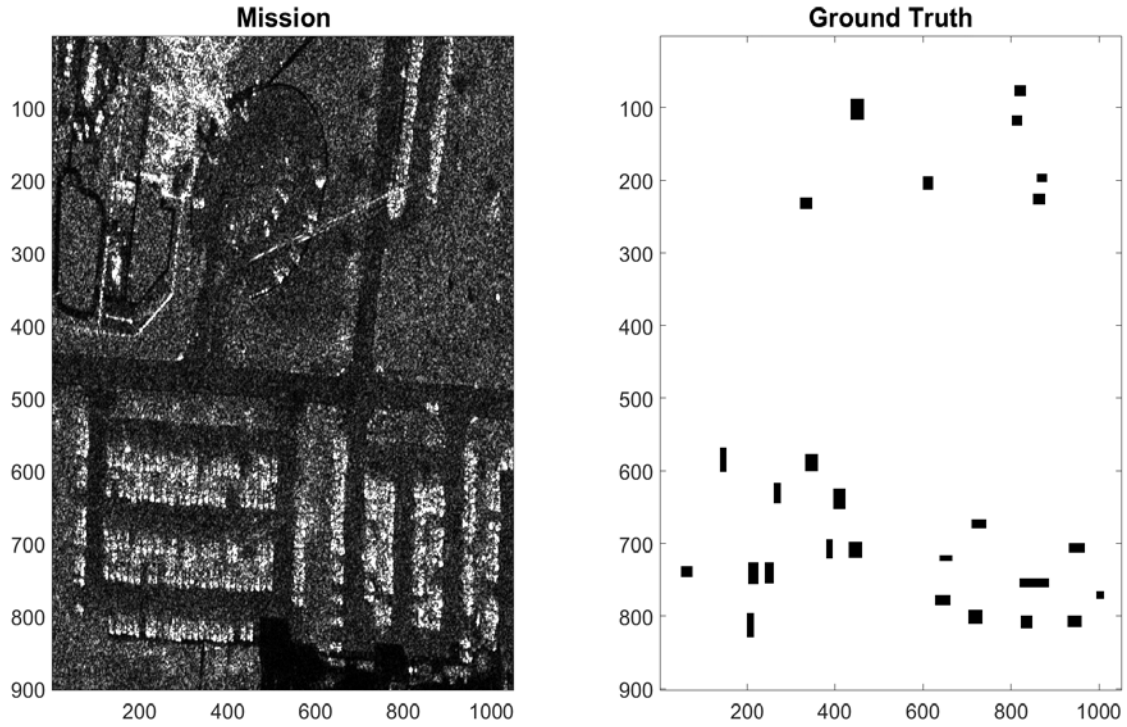


Figure 23. Mission Image Comparison to Ground Truth

During the investigation, we noticed a high false alarm rate when evaluating the CCD challenge dataset. This is due to the sliding window’s natural behavior of causing “bleed over” into adjacent pixel boxes around targets. A method exists to extend the ground truth boxes to account for this bleed over. This is called guard cells and was used in [19]. In addition to the sliding window’s behavior in this thesis research, energy spillover is mentioned to be a factor in bleed over as well. The size of the guard cells in this thesis research was five pixels in width and height. This extends the boxes by ten pixels in width and ten pixels in height. By including the guard cells, the false alarm rate decreased. The ground truth with the extended guard cells is shown in Figure 24. The ground truth is shown in the left panel, and the extended guard cells are given in the right panel.

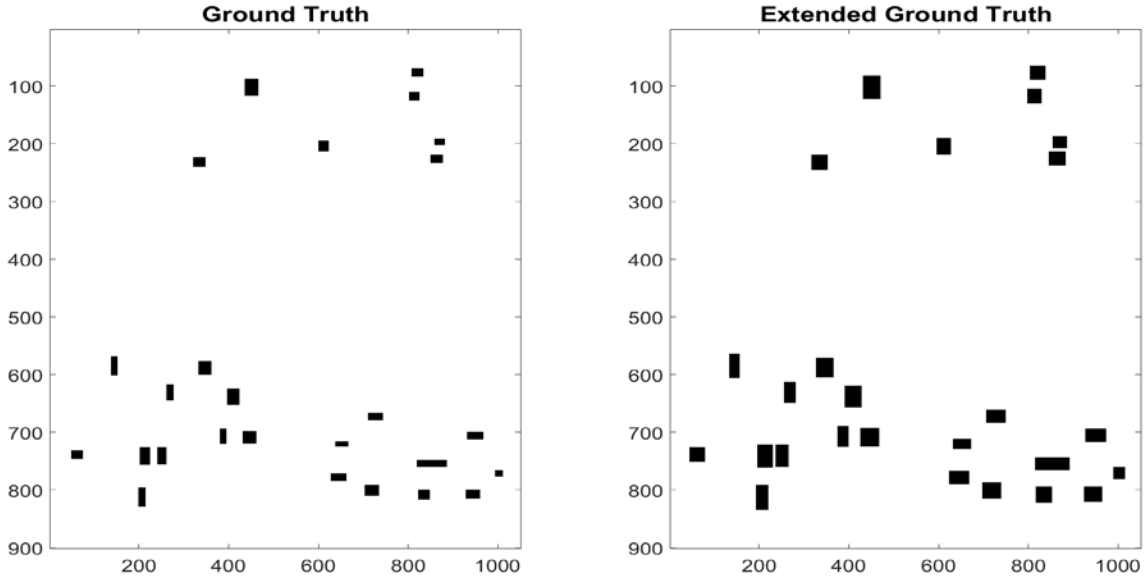


Figure 24. Ground Truth versus Extended Guard Cells

In later sections of this chapter, there are comparisons to other changes that are noticed in the pair of images during CCD application. This is due to the CCD's ability to recognize small-scale changes. These are not included in the ground truth images because these changes cannot be discerned visually; however, qualitative analysis is done on the circular track described in Chapter VI Section A.

A zoomed-in area of the subarea is shown in Figure 25. The image was created using ICCD change detection. The size of the red box in the image is 28 by 12 pixels. Using Equation (39), we calculated the size to be 6.44 m by 2.76 m. This is approximately 2.4 times longer and 1.5 times wider than the average mid-size sedan size in Table 2. This result could be affected by the bleed-over effect and energy spillover. Applying additional averaging will extend the size even more.

An example of a suspected car change is presented in Figure 25. The left and right subfigures show the mission and reference images, respectively. White represents a change was detected and black represents no change. An assumed shape for a car detection is rectangular in nature; however, the change region in the reference subfigure does not have a definitive shape. This example figure is to illustrate the difficulty of labeling change through visual inspection.



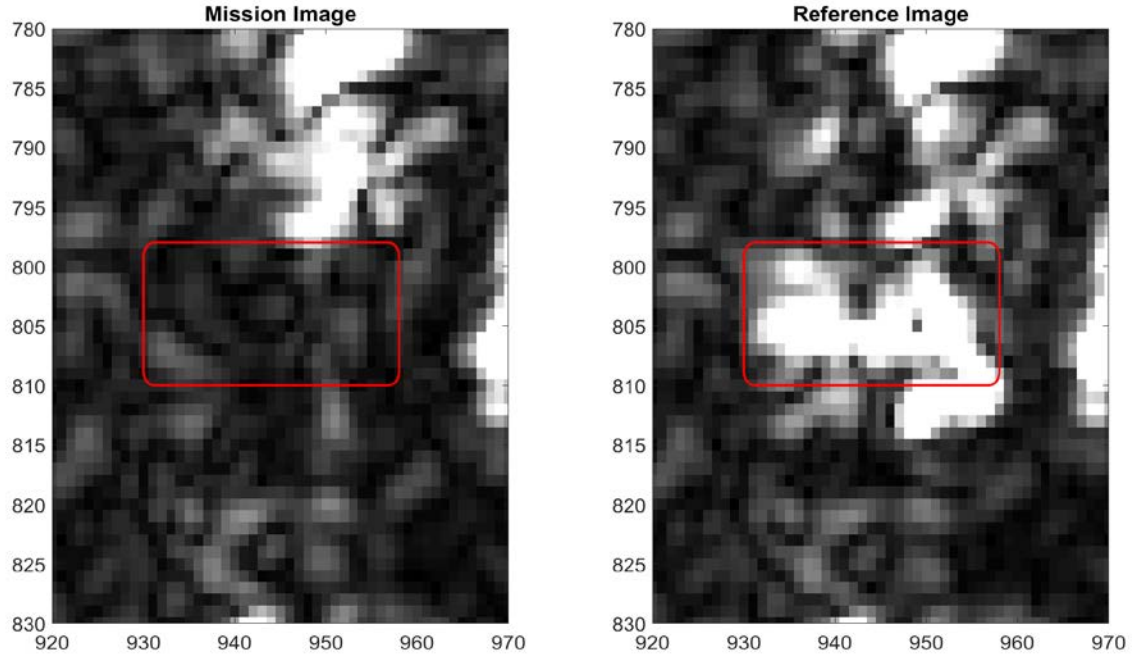


Figure 25. Zoomed-in Area of Suspected Car

### C. ICCD VERSUS CCD RESULTS

Before showing the quantitative ROC curves, the raw output of these filters are placed side by side to show qualitative differences in behavior in Figure 26. For the ICCD outputs, the large-scale changes are recognized well. Large-scale change in the context of this investigation means cars moving, large ground changes, e.g., fields being plowed. To iterate, large-scale changes are on the order of tens of meters.

For small-scale changes, the CCD outperforms the ICCD method in Figure 26. The ICCD and CCD outputs are in the left and right subfigures, respectively. The ICCD has visible noise through its output. Small-scale changes are on the order of a few meters, such as a gravel track being used in between passes. As shown in the red circle, the track area is discerned clearly in the CCD output. The track area in the ICCD output is cloudy from the speckle and appears to blend into other surrounding pixels; however, the CCD visual change does not have a low coherence. From the color bar, the track is  $\sim 0.5$  coherence. Usually a good value of estimated coherence is closer to 0.2 or less.

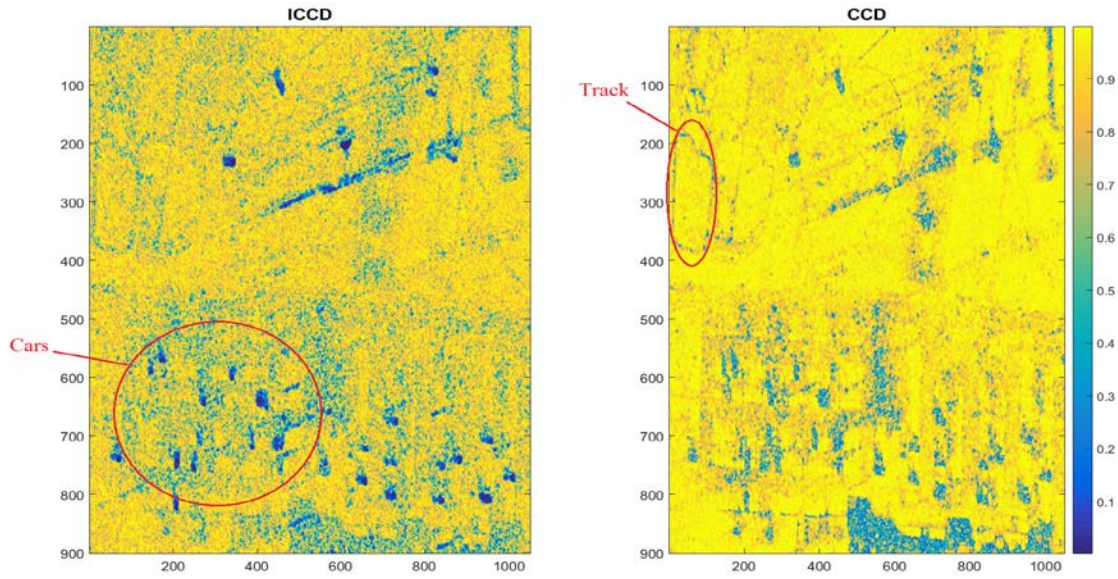


Figure 26. ICCD and CCD Subarea Results

The track area in Figure 26 is focused and presented in Figure 27. The purpose of Figure 27 is to clearly show the speckling effect on the ICCD and the better performance of the CCD.

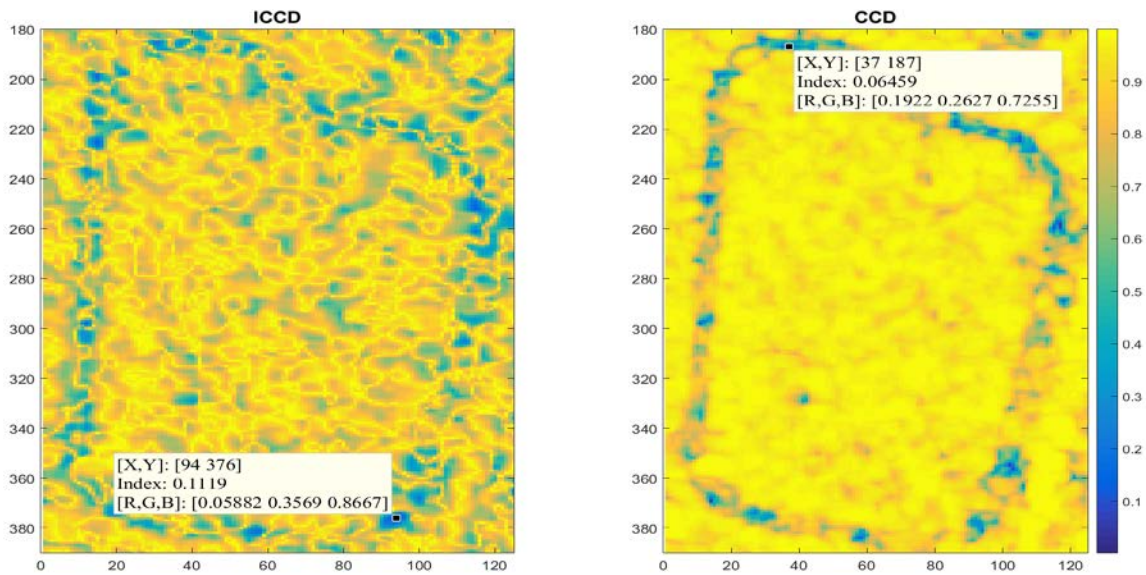


Figure 27. Track Area of Figure 26

The ICCD change statistic is 1.73 times the CCD change statistic value, calculated by the ratio of the data points in Figure 27. The CCD figure has a less-noisy background than the ICCD. The noise does affect the ICCD change statistic.

On the north-side part of the track, there is less coherence than the south-side. This change may have been induced by someone walking on the track in between the times of capture for the mission and reference image. Furthermore, the track could be made of gravel causing slightly different scattering properties to the scene if heavily used.

The cars have more distinction when using the ICCD method. From Figure 28, the ratio of the data tips indices is 39. This is indicative of the ICCD performance over CCD for recognition of large objects. The noise is not apparent in the ICCD image of the car locations, indicating a large disturbance affected the mean backscatter of the repeat pass images.

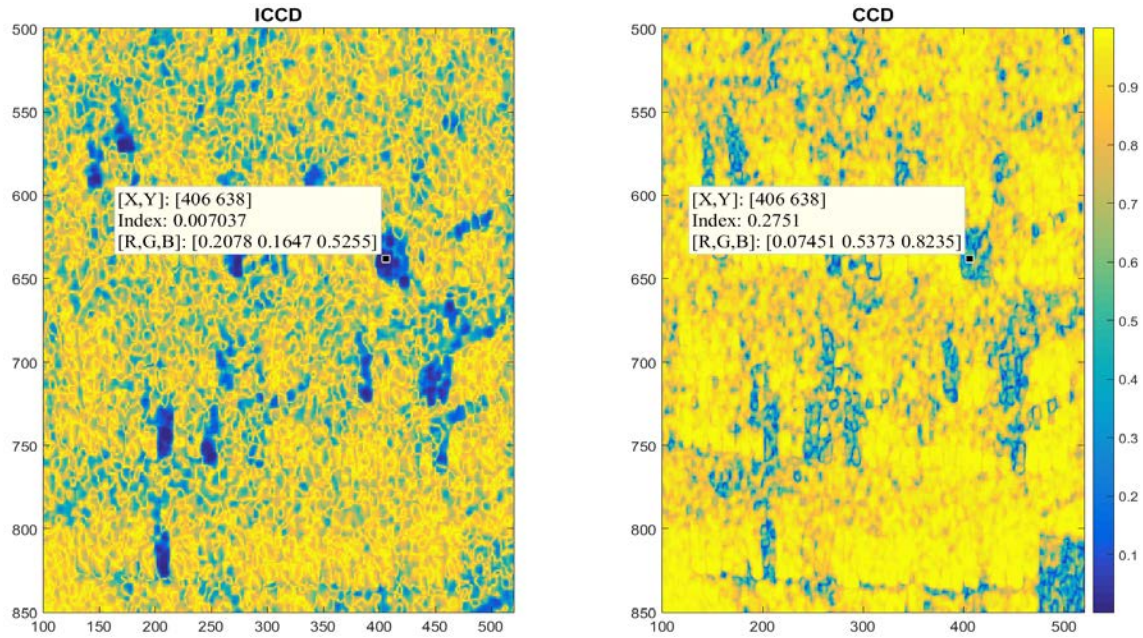


Figure 28. Zoomed-in Car Area of Figure 26

To illustrate the difference in performance in more quantitative terms, the ROC curve is presented in Figure 29. The crossover point where CCD starts to outperform the ICCD is for a detection threshold of 0.515.



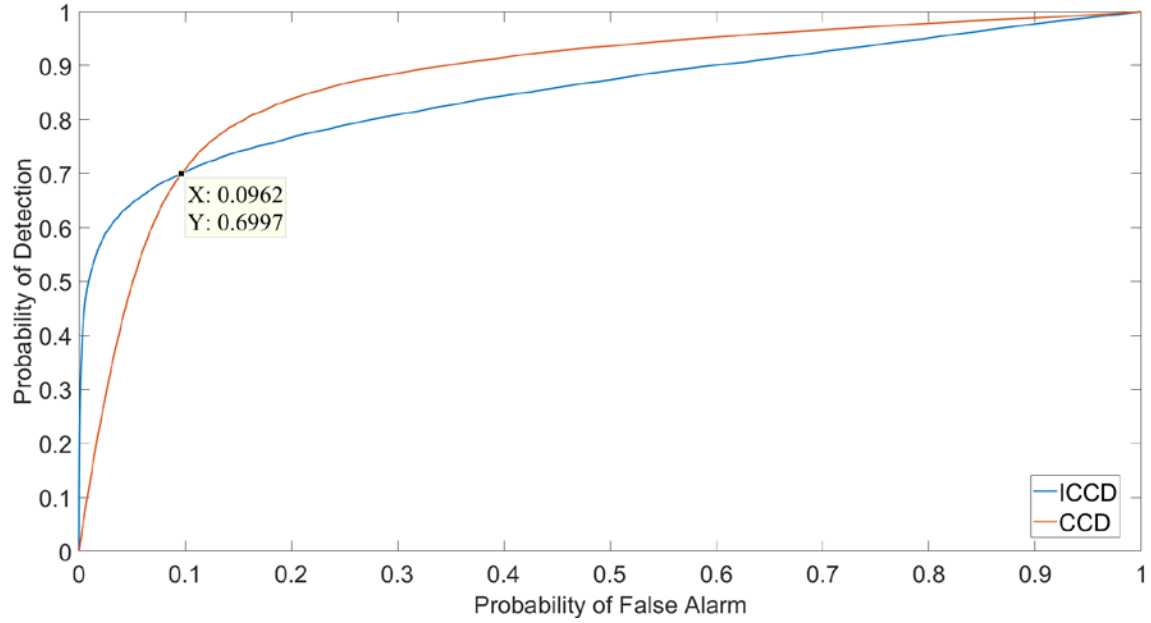


Figure 29. ROC Curve for ICCD versus CCD

The ICCD change map, CCD change map, and ground truth is shown in Figure 30. The black dots represent change and the white dots represent no change. In these plots, the binary change maps are given for  $N = 5$  and  $T = 0.515$ .

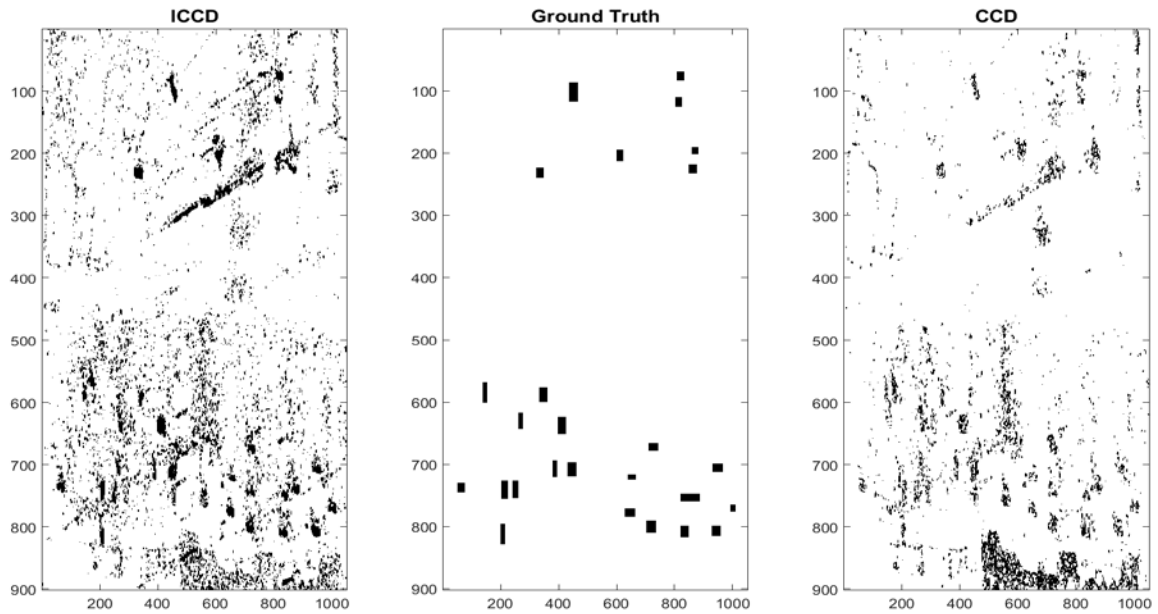


Figure 30. ICCD versus CCD Binary Change Maps with Ground Truth

The ICCD was better visually than the CCD. The binary change masks in Figure 30 illustrates this point. Outside the ground truth boxes, there are significant large artifacts that appear in the ICCD change map. In contrast, the ICCD identifies change pixels more quickly than the CCD, but the inherent noisy nature weighs down its performance over the threshold range.

#### D. ACCD VERSUS CCD RESULTS

The ACCD method is measured against the CCD method in this section. The ACCD method has superior performance when the underlying backscatter repeat-pass images are approximately equal. In this context, fewer false alarms occur. Since the images are already registered, the backscatter powers in the unchanged areas of the scene should be similar. Any large differences in backscatter power should only be the changed areas. The raw outputs of the ACCD and CCD methods of the area of interest are displayed in Figure 31. The left and right panels provide a comparison of ACCD versus CCD raw outputs for an area of interest.

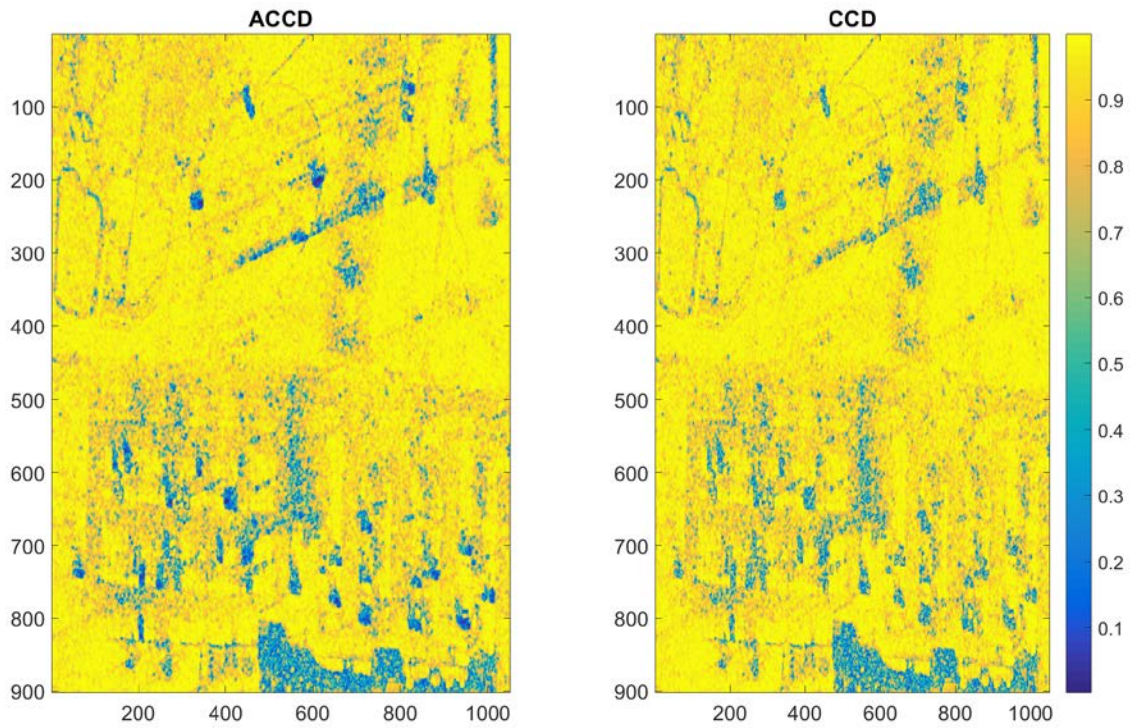


Figure 31. Area of Interest with ACCD versus CCD Raw Outputs

Use of the denominators in Equations (8) and (9) within Equation (4) yields

$$A = \sqrt{I_f I_g}, \quad (40)$$

and

$$B = \frac{I_f + I_g}{2}. \quad (41)$$

Inspecting the altered denominators, Equation (40) is the multiplication of the intensities of a local neighborhood, and Equation (41) is the sum of the intensities of the repeat-pass pair. An assumption of the underlying backscatter power approximately being equal in areas of no change implies Equation (41) as the more stable of the two equations.

Continuing with the investigation, we compare the ACCD and CCD performance of the cars in Figure 32. It is important to note that vehicles are more pronounced in the ACCD raw output. The CCD denominator, Equation (40), experiences a multiplicative effect that impacts the coherence value.

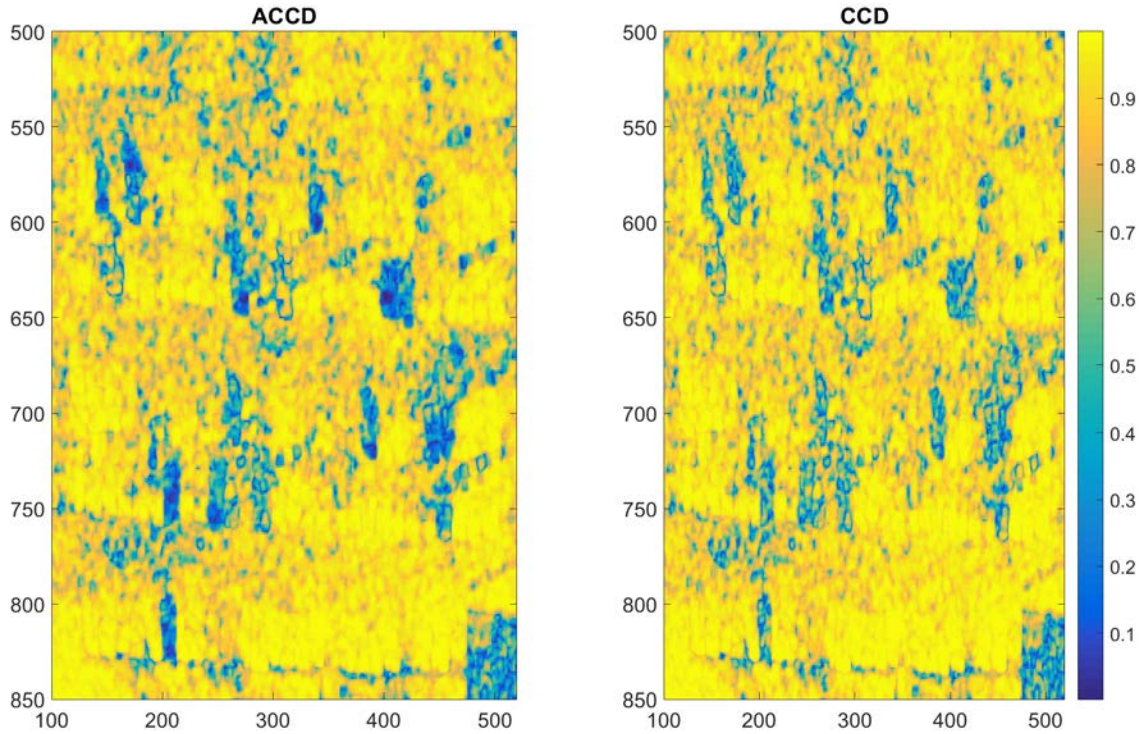


Figure 32. Zoomed-in Car Area ACCD versus CCD Change Detection Methods

The ROC characteristics of these two methods are similar, as shown in Figure 33; however, the ACCD outperforms the CCD for high threshold values. The ACCD does not converge with the CCD curve until a  $P_{fa}$  of 0.65. At this point, the thresholds are very low, allowing for more noise to be registered as changes.

Earlier, it was stated that the ACCD should outperform the CCD based on the knowledge of the dataset having similar underlying backscatter power. Indeed, there may be cases where the CCD method has better performance than the ACCD. To no avail, there are zero instances when the CCD outperformed the ACCD in this research.

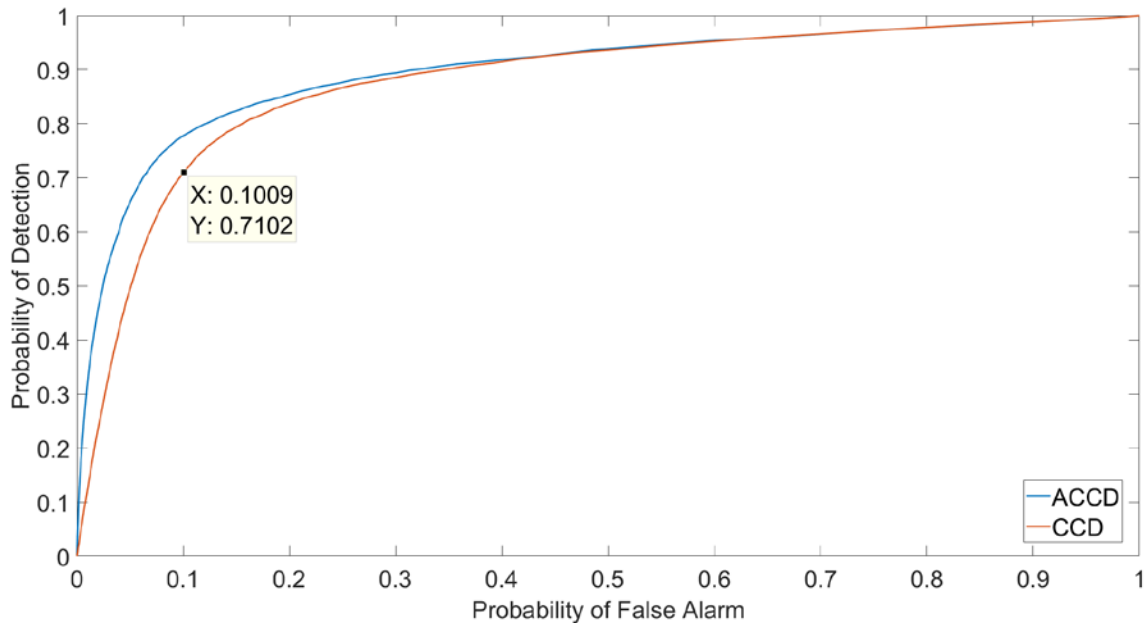


Figure 33. ROC Curve for ACCD versus CCD

The binary change maps are generated with a threshold of  $T = 0.705$  and  $N = 5$  in Figure 34. The noise behavior of the ACCD and CCD outputs are similar except for the ground truth areas. The ACCD detection in the ground truth areas are filled in more, as seen by the solid black, whereas the CCD ground truth region has grainy shapes and discerning a target is not clearly achieved.

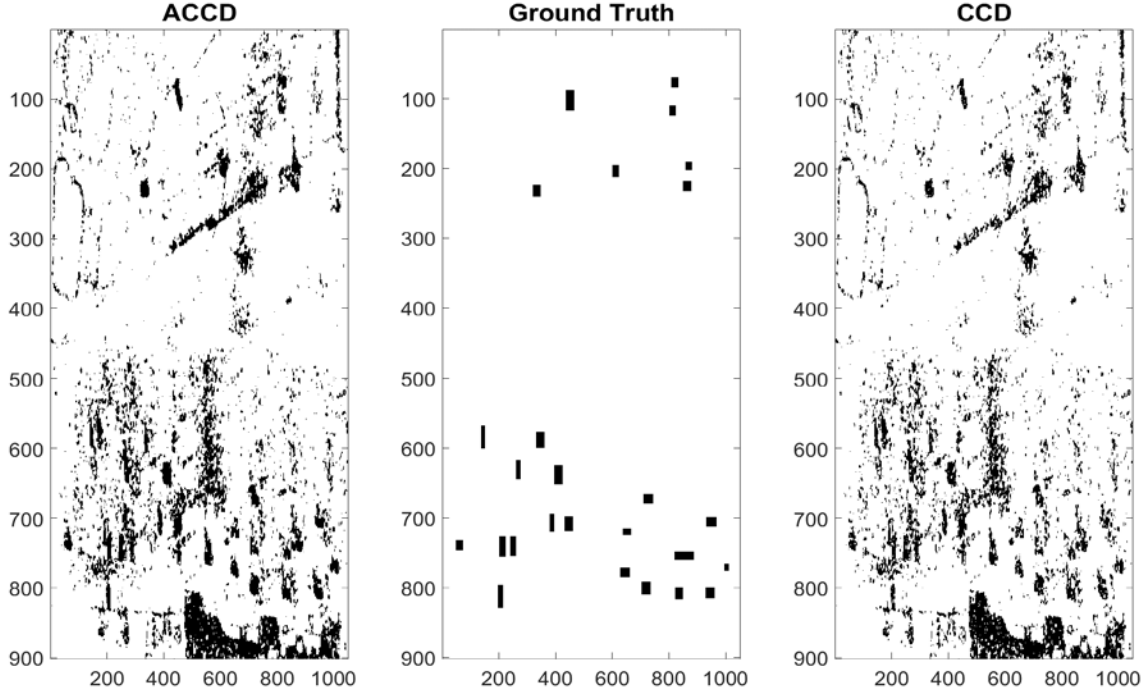


Figure 34. ACCD versus CCD Binary Change Maps with Ground Truth

## E. LLCS RESULTS

The LLCS results presented in this section are for single polarization. Having the additional polarizations improves the results; however, the results presented here are to capture the base performance of the LLCS method and not the polarimetric extension.

The LLCS detector performs best with knowledge of the true covariance matrices of the images. Since the true characteristics of the scenes are not known, approximations are made for the  $\underline{Q}$  matrices. A pair of maximum-likelihood estimators [9] replace the  $\underline{Q}$  matrices in Equations (12) and (13) as

$$\hat{\underline{Q}}_0 = \frac{1}{M_0} \sum_{k=1}^{M_0} \underline{X}_{k_0} \underline{X}_{k_0}^H, \quad (42)$$

and

$$\hat{\underline{Q}}_1 = \frac{1}{M_1} \sum_{k=1}^{M_1} \underline{X}_{k_1} \underline{X}_{k_1}^H, \quad (43)$$



Here,  $M_1$  and  $M_0$  are the number of pixels in the estimate,  $\underline{X}_{k_0}$  and  $\underline{X}_{k_1}$  are the column image vectors pairs defined, respectively, as

$$\underline{X}_{k_0} = [f_{k_0}, g_{k_0}]^T \quad (44)$$

and

$$\underline{X}_{k_1} = [f_{k_1}, g_{k_1}]^T, \quad (45)$$

where  $k = 1..M$  and  $M$  is  $M_0$  or  $M_1$  is from Equation (42) or Equation (43), and  $f$  and  $g$  are the image pixels from the reference image and repeat image, respectively. The subscript 0 and 1 refer to the null hypothesis  $H_0$  and the alternate hypothesis  $H_1$ .

The area of consideration in the prior sections is not used here. Instead, a focused area that includes a car-like object with surroundings of grass and trees was used. The LLCS uses the estimators from Equations (42) and (43). The image pairs are found using the ground truth from Chapter VI Section B. The parameters  $M_1$  and  $M_0$  were set to 414 and 50547, respectively. The LLCS results are compared with the CCD and ICCD results are shown in Figure 35. The units of the LLCS and ICCD color bars are in dB. The CCD color bar values are dimensionless and represent coherence.

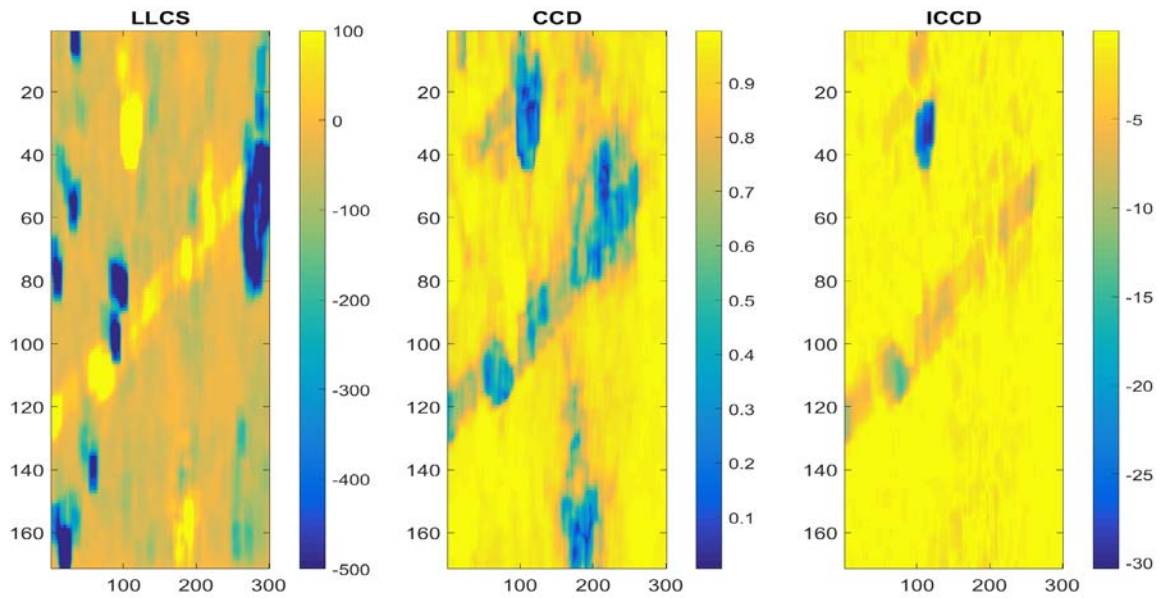


Figure 35. LLCS versus CCD versus ICCD Single Car Results

The LLCS is expected to be far superior to the ICCD and CCD algorithms; however, there are more visible artifacts seen in the LLCS subfigure in Figure 35 than the ICCD or CCD subfigures. The single car can be seen clearly in the ICCD output. The CCD subfigure shows the car along with a diagonal line artifact. The LLCS filter does not perform as expected. This could be due to error in how the estimation is formed or not having the images properly registered.

The ROC curves show more clearly the performance results of the three methods in Figure 36. The LLCS trends with the ICCD curve, while the CCD performs poorly next to these two. At a  $P_d$  of approximately 0.9 the ICCD and LLCS have a  $P_{fa}$  of 0.0007. The CCD method has a  $P_{fa}$  of 0.064. The  $P_{fa}$  values have two orders of magnitude difference.

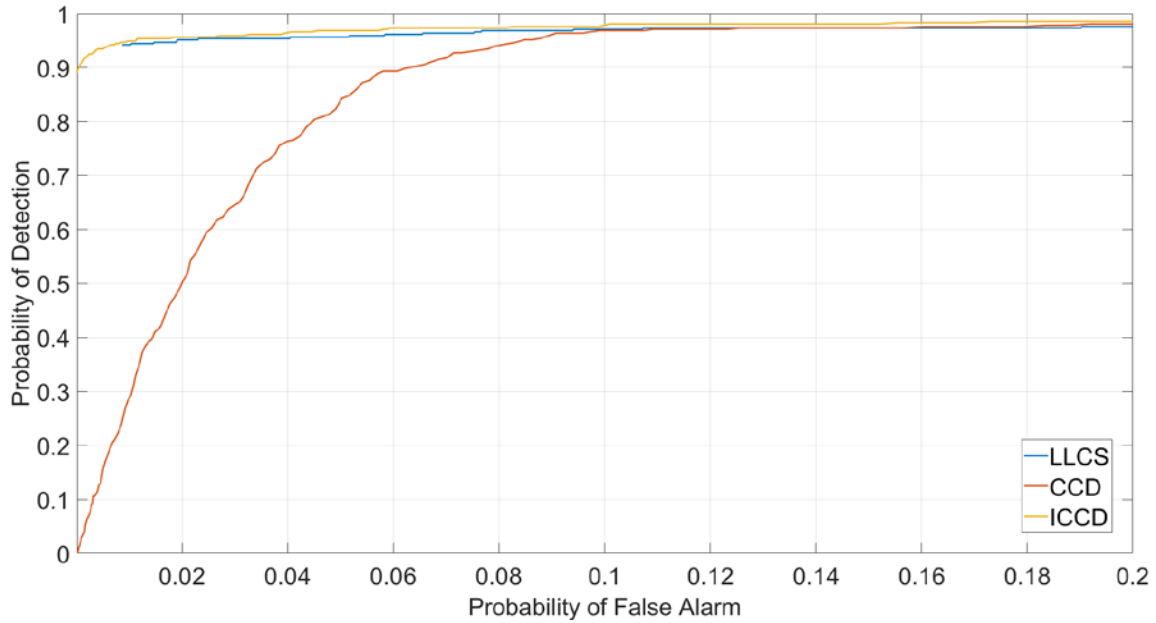


Figure 36. ROC Curves for CCD versus ICCD versus LLCS

The results of the LLCS change detection are a cause for concern. The ICCD seemed to perform better than or as well as the LLCS. Another author has similar results to the ICCD and CCD for the CCD challenge problem [20], as shown in Figure 37.

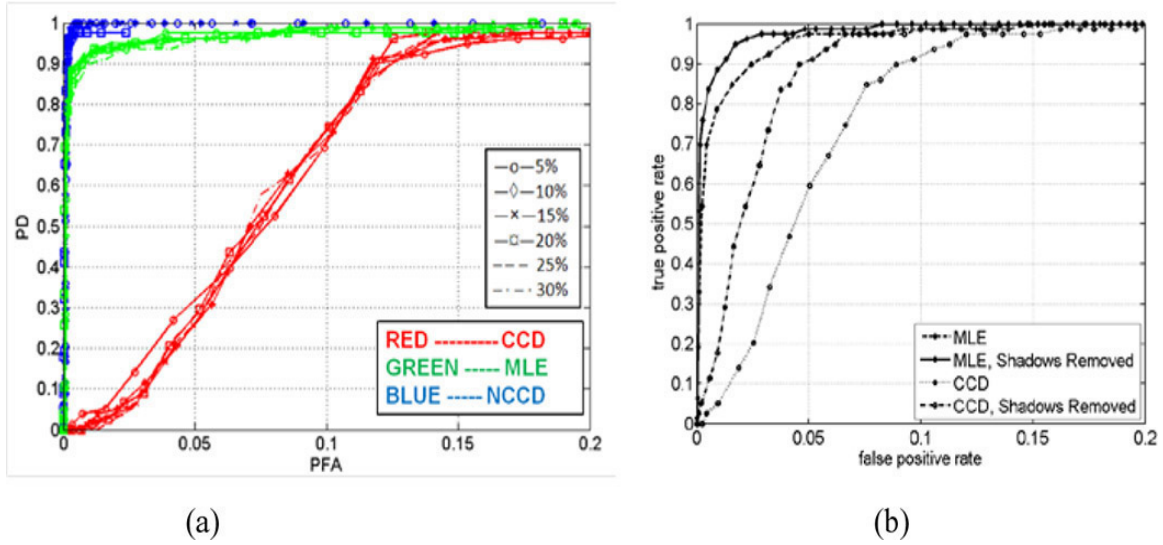


Figure 37. Change Detection ROCs. Source: [20].

## F. TWO-STAGE RESULTS

The two-stage filter is a composite filter involving the ACCD and the ICCD methods so its results should be similar to both. The two-stage filter raw output has more discernable changes than the ACCD algorithm, as shown in Figure 38. This improvement to output can be attributed to the ICCD inclusion into the filter.

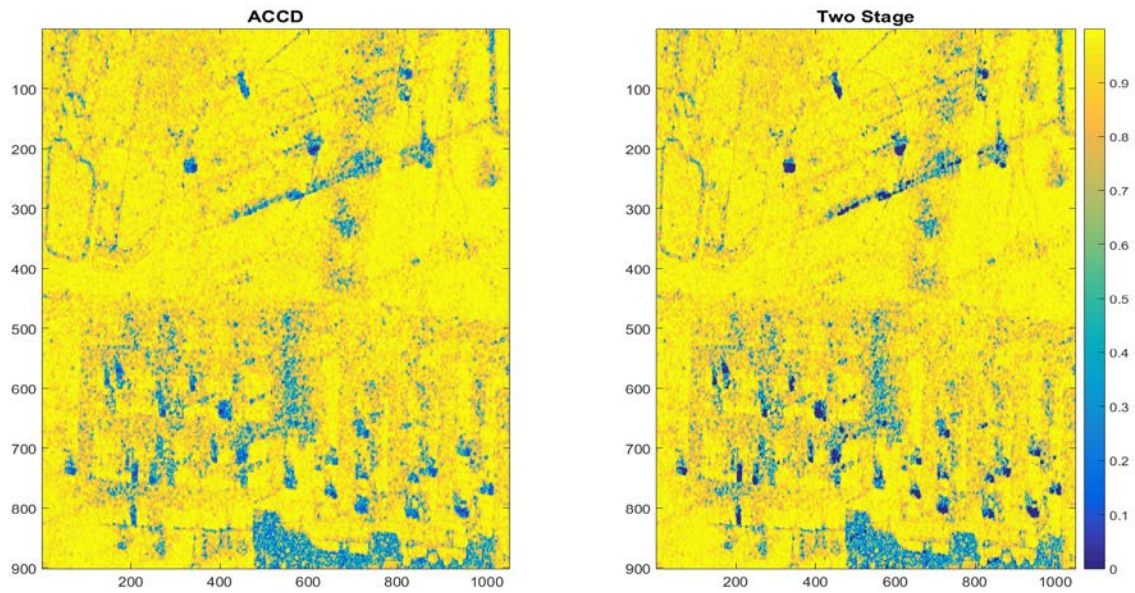


Figure 38. ACCD versus Two-Stage Raw Output

The running track area in the subfigure for the two-stage filter is quite identical to the ACCD output. The two figures are nearly the same. For the areas of car change detection, there is deeper blue indicating a better registration of change from the two-stage filter. This was not an area of the ground truth but shows the effects of the CCD algorithms of reducing speckle.

The zoomed-in track area is presented in Figure 39. The two-stage filter did not suffer as much noise as the ICCD filter. This is from the benefit of the ACCD. The deeper blues can be seen in the Two-Stage subfigure showing an improvement over ACCD.

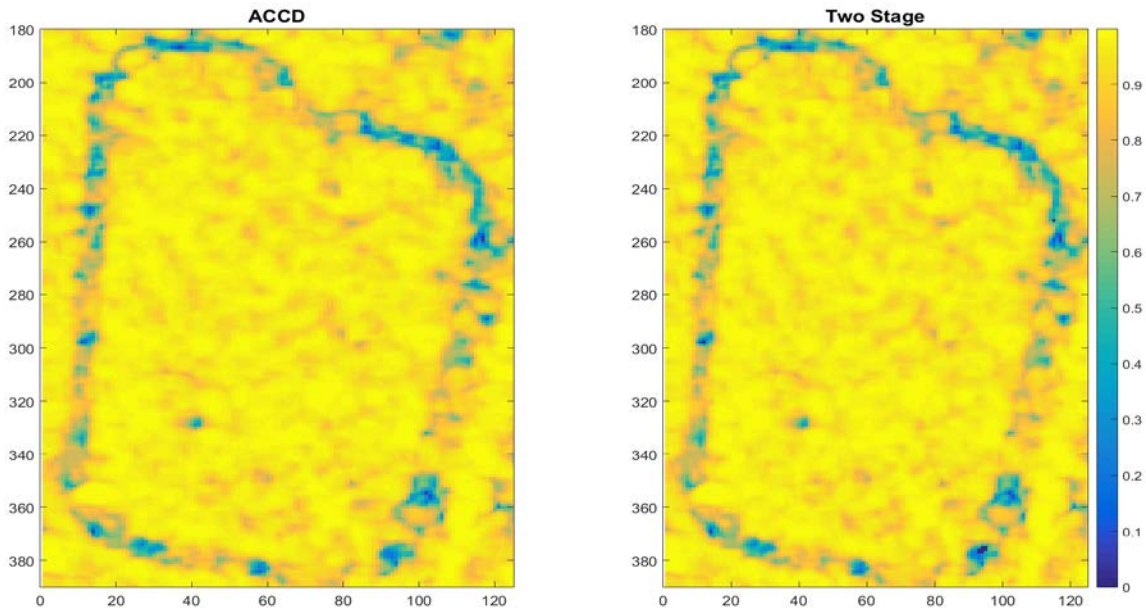


Figure 39. ACCD versus Two-Stage Track Areas

The ICCD car area from Figure 28 was improved upon using the two-stage change detection. The two-stage method created rounded images for the cars in Figure 40. Furthermore, the amount of speckle around the car areas was reduced, which leads to a reduction in the number of false alarms. The reduction of speckle from the ICCD output of the two-stage filter is due to the null hypothesis test.



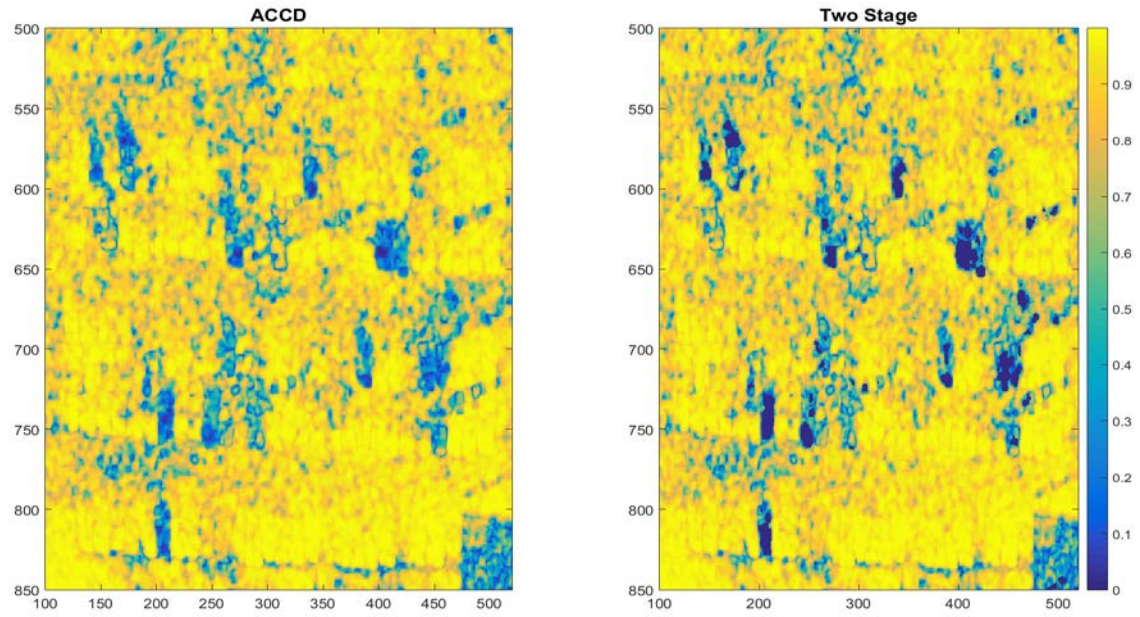


Figure 40. ACCD versus Two-Stage Car Areas

The two-stage ROC curve is presented with the ACCD and ICCD as a comparison to the two-stage filter, as seen in Figure 41. At a  $P_{fa}$  of approximately 0.05, the three filters converge in the ROC graph.

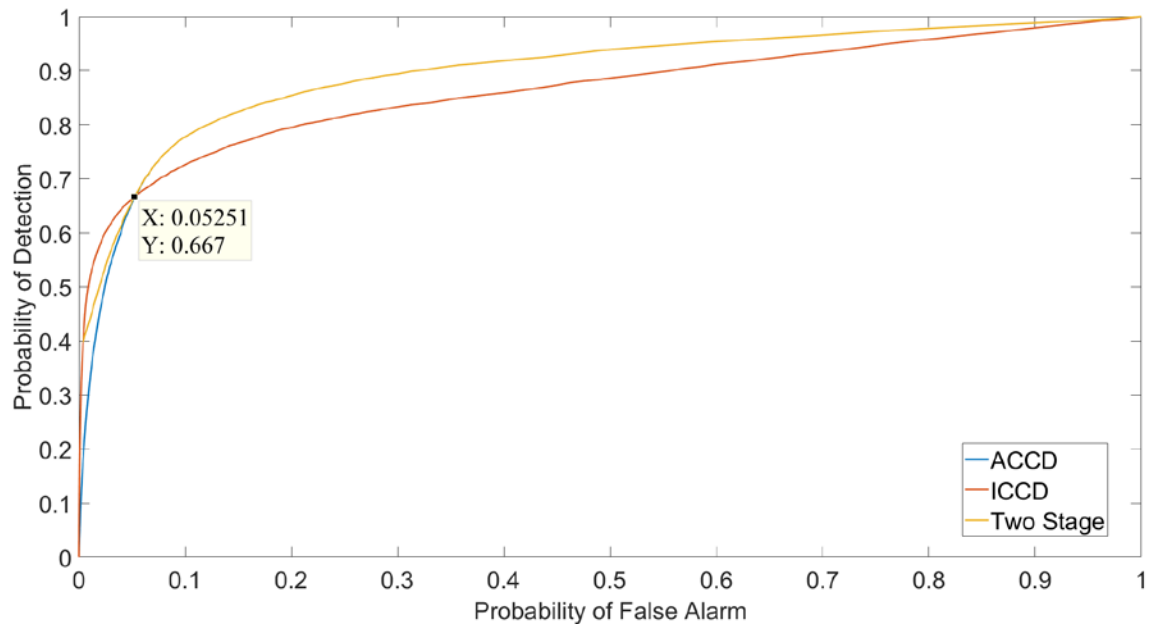


Figure 41. ROC Curves of ACCD, ICCD, and Two-Stage Filters

As mentioned previously, the basic ICCD in Chapter III Section A does not use the null hypothesis test. This allows for more contribution from speckle that will affect the coherence. After the crossover near a  $P_{fa}$  of approximately 0.05, the two stage begins outperforming the ICCD algorithm for higher  $P_{fa}$  values but runs in parallel to the ACCD ROC curve. This is to be expected since the second stage is entirely the ACCD method.

The binary map was generated with a threshold of 0.46 for a  $P_{fa}$  of 0.05, as shown in Figure 42. The white represents no change and black represents change. On the bottom of the left and right subfigures there is a large change area that is not a part of the ground truth, the area inside the red box. This region is assumed to be trees or foliage. This result is shown to be filtered out in the next section. Reduction of these false alarms can be achieved by post processing operations. This was not pursued in this investigation; however, this area is responsible for raising the  $P_{fa}$  in the ROC curves of Figure 41. The ACCD and Two-Stage binary change maps were generated with  $N = 5$  and  $T = 0.46$ .

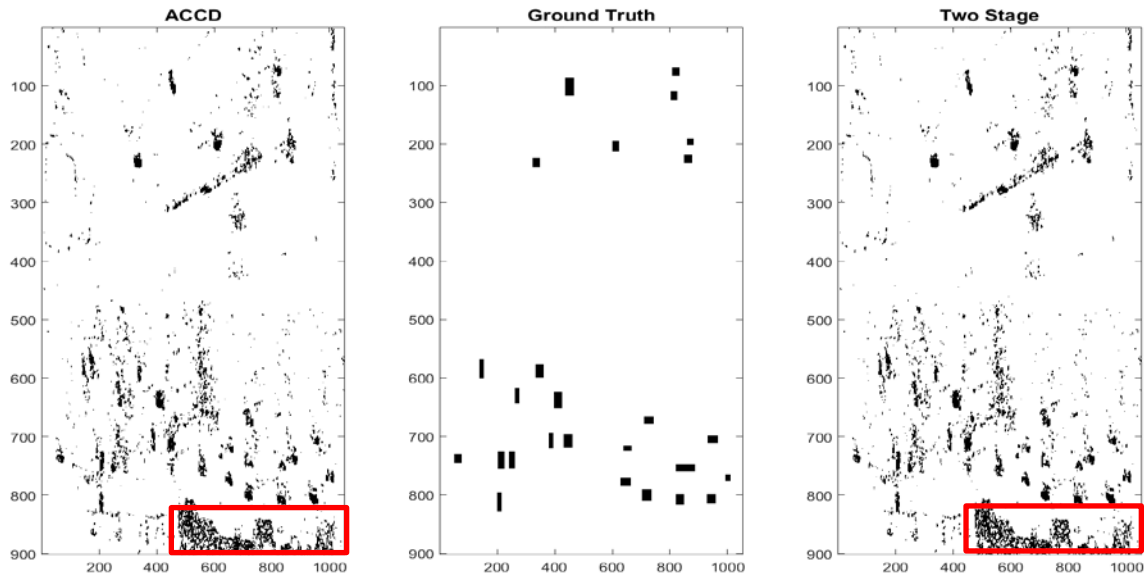


Figure 42. ACCD and Two-Stage Comparison to Ground Truth

## G. THREE-STAGE CHANGE DETECTION RESULTS

The three-stage filter is only compared to the single polarization LLCS and the two-stage filter. The premise is that the three-stage filter would show improvement over the LLCS method. For the comparison of the two stage and three stage methods, it was hypothesized that the three-stage filter would have equivalent or better performance. Visually, the three-stage method yields higher performance than the LLCS and two-stage methods; however, this conclusion does not apply to the quantifiable results.

The three-stage filter yielded more promising visual results than that of the single polarization LLCS. The visual results of these two filters are shown in Figure 43. The artifacts are overwhelming in the single polarization LLCS subfigure; whereas, the three-stage filter shows a noticeable reduction in the amount of speckled noise. For example, the road edges can be seen in the three stage's results clearly. The LLCS speckle distorts the edges of the road and other characteristics of the scene.

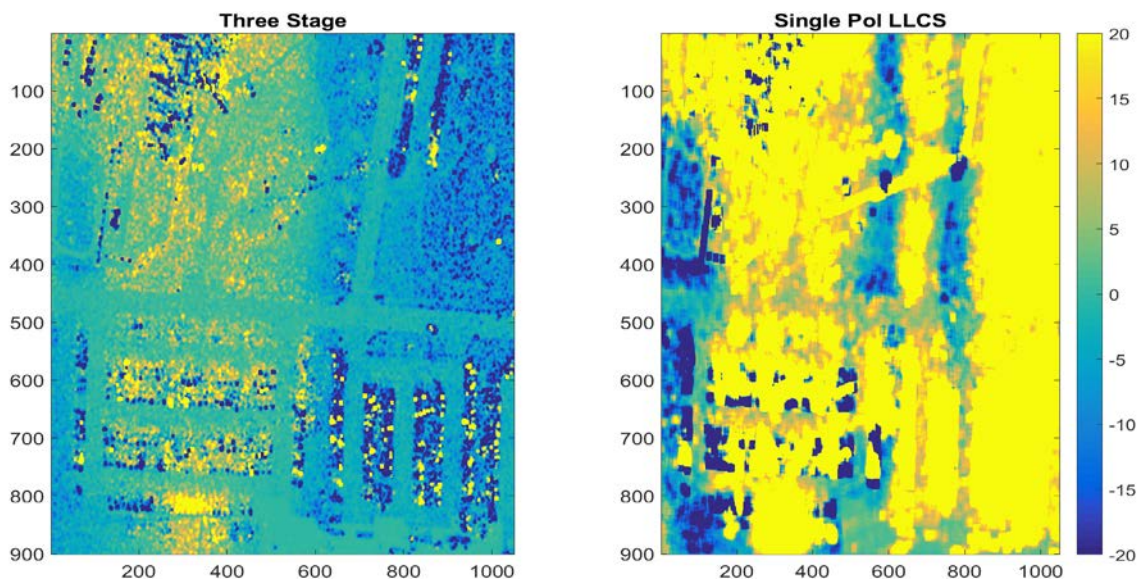


Figure 43. LLCS versus Three-Stage LLCS Output

Even though the visual quality of the three-stage filter is clearly better than that of the LLCS, the ROC curves contradict the visual successes. The starting point of the LLCS curve in Figure 44 is at a higher  $P_d$  than the three-stage filter; however, the binary

operation results of the three-stage filter are satisfactory. The binary change masks are seen in Figure 45.

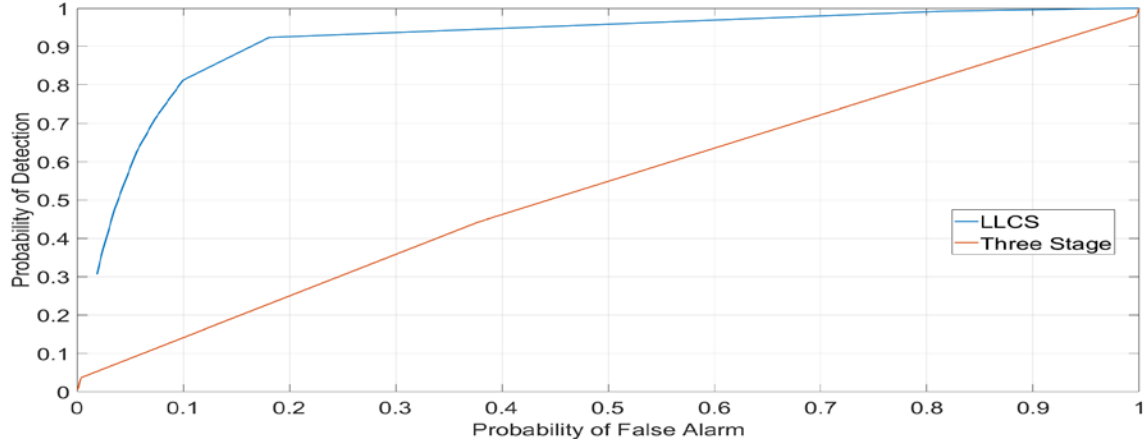


Figure 44. ROC Curves for LLCS versus Three Stage

The three-stage results of Figures 41 and 42 did not incorporate the binary operations. The binary operations were included only in Figure 45. The three-stage results used a  $z$  threshold of 80 dB for the LLCS stage. For the two-stage filter, the threshold for the coherence was set to 0.9, and alpha was set equal to 0.01 for the null hypothesis test.

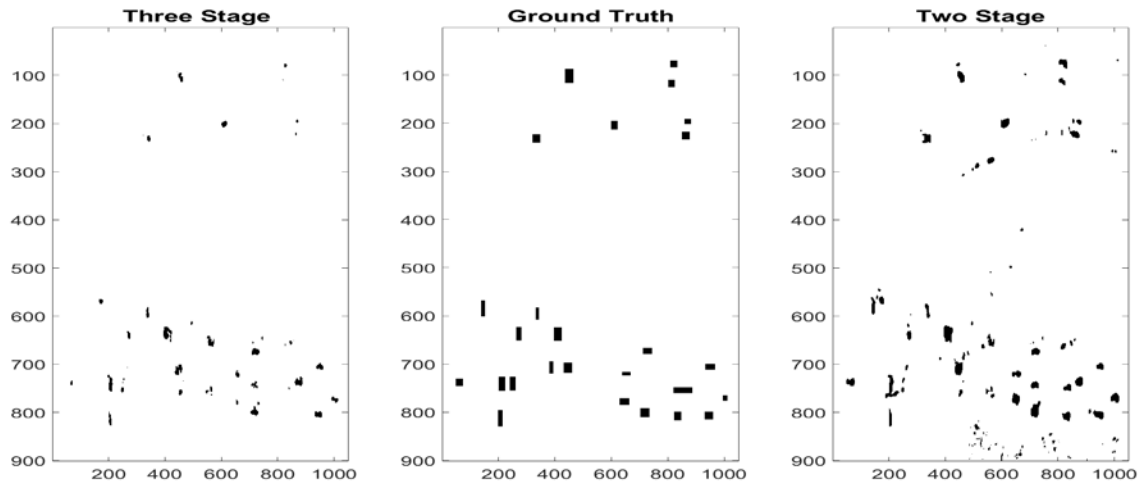


Figure 45. Change Masks of Three Stage, Two Stage Change Mask, and Ground Truth



## VII. CONCLUSIONS

### A. DISCUSSION OF RESULTS

In this investigation, six change detection methods were studied and analyzed. A number of visual and quantitative comparisons were shown and led to greater understanding of the change detection filters' strengths and weaknesses. The ICCD performance was superior at identifying large-scale changes with lower thresholds than other methods. The ACCD could identify small-scale changes just as well as the CCD. Also, the ACCD method rendered large-scale changes clearer than the CCD method.

The LLCS detector was expected to be the superior change detection method in this method; however, the LLCS results were only superior in the simulator results. For the application to the CCD challenge problem dataset, the LLCS had equivalent results to the ICCD and CCD methods, seen in Figure 36. This implies the estimation of the  $Q$  matrices could have errors in implementation.

The CCD challenge dataset results were surprising as well. The change detection method that had the best ROC curve was the two-stage filter. In addition, the visuals showed clear change in the ground truth regions seen in Figures 40 and 42.

The three-stage filter showed high detail of the scene but had the worst ROC curve. The three-stage delineated roads from surrounding grass areas and the cars from the parking lot, seen in Figure 43. The poor ROC curve performance is from more false alarms than the other methods. The three-stage was indeed hoped to have the best performance but fell short; however, the design and implementation of the three-stage filter was a good venture.

### B. FUTURE WORK

There are a number of possible avenues for valuable analyses which could follow the current investigation. First, the LLCS theory and the incorporation of the LLCS change detection method into MATLAB could be improved. The execution time of the LLCS algorithm was on the order of minutes. The Two-Stage, CCD, ACCD, and the

ICCD algorithms executed on the order of seconds. The LLCS equations were ported directly into MATLAB without any simplification for computational efficiency.

The Three-Stage change detection Q estimate is believed to be at fault for the poor performance. A better method of estimation is needed for this algorithm to be successful. A method to improve upon this Q estimate would be to do a spline fit to the scene such as in [13]. An additional point of study would be how to increase performance of the change detection methods, such as in [4], by using eigenvalue methods instead of the simple threshold detector used in this investigation.

An unstated point to this investigation for the author was to determine if there was a change detection method that performed well in most circumstances. Based on the results, the two-stage filter or the ACCD change detection are suitable candidates.

## LIST OF REFERENCES

- [1] C. A. Wiley, "Synthetic aperture radars," in *IEEE-Transactions on Aerospace and Electronic Systems*, vol. AES-21, no. 3, pp. 440–443, May 1985. [Online]. Available: <http://ieeexplore.ieee.org/document/4104077/>
- [2] Y. Zhang and X. Cheng, "Application of SRTM-DEM based two-pass SAR interferometry for detecting seismic deformation on high-altitude rugged terrain—A case study in Kokoxili Ms8.1 earthquake, 2001," in *Geoscience and Remote Sensing Symposium*, 2005, vol. 7, pp. 5316–5319.
- [3] J. Stastny, M. Hughes, D. Garcia, B. Bagnall, K. Pifko, H. Buck, and E. Sharghi, "A novel adaptive synthetic aperture radar ship detection system," in *OCEANS*, 2011, pp.1–7
- [4] V. Carotenuto, A. D. Maio, C. Clemente, J. J. Soraghan, and G. Alfano, "Invariant rules for multipolarization SAR change detection," *IEEE Trans. on Geosci. and Remote Sens.*, vol. 53, pp. 3294–3311, Dec. 2014.
- [5] R. Touzi, A. Lopes, and P. Bousquet. "A statistical and geometrical edge detector for SAR images," *IEEE Trans. on Geosci. and Remote Sens.*, vol. 26, pp. 764–773, Nov. 1988.
- [6] M. Cha, R. D. Phillips, P. J. Wolfe, and C. D. Richmond, "Two-stage change detection for synthetic aperture radar," *IEEE Trans. on Geosci. and Remote Sens.*, vol. 53, pp. 6547–6560, July 2015.
- [7] The Sensor Data Management System. (n.d.). Object name: A challenge problem for SAR change detection and data compression. [Online]. Available: <https://www.sdms.afrl.af.mil/>. Accessed June. 15, 2016.
- [8] S. M. Scarborough, L. Gorham, M. J. Minardi, U. K. Majumder, M. G. Judge, L. Moore, L. Novak, S. Jaroszewski, L. Spoldi, and A. Pieramico, "A challenge problem for SAR change detection and data compression," *SPIE Proceedings*, vol. 7699, Apr. 2010. doi: 10.1117/12.855378
- [9] M. Preiss and N. J. S. Stacy, "Coherent change detection: Theoretical description and experimental results," Def. Sci. and Tech. Org., Edinburgh, South Australia, Rep. DSTO-TR-1851, August 2006.
- [10] A. Bouaraba, A. Younsi, A. Belhadj-Aissa, M. Acheroy, N. Milisavljevic, and D. Closson, "Robust techniques for coherent change detection using COSMO-skymed SAR images," *Progress in Electromagnetics Research*, vol. 22, pp. 219, 2012.

- [11] C. A. Balanis, *Antenna Theory Analysis and Design*, 2nd ed. Hoboken, NJ: John Wiley & Sons, 2005.
- [12] M. Preiss and N. J. S. Stacy, "Polarimetric SAR Coherent Change Detection," in 7<sup>th</sup> European Conference on Synthetic Aperture Radar, Friedrichshafen, Germany, 2008.
- [13] M. Preiss, D. A. Gray, and N. J. S. Stacy, "Detecting scene changes using synthetic aperture radar interferometry," *IEEE Trans. on Geosci. and Remote Sens.*, vol. 44, pp. 2041–2054, 2006.
- [14] D. Arthur and S. Vassilvitskii, "K-means++: The advantages of careful seeding," in *Proceedings of the Eighteenth Annual ACM-SIAM Symposium on Discrete Algorithms*, New Orleans, LA, 2007, pp. 1027–1035.
- [15] B. R. Mahafza, *Radar Systems Analysis and Design Using Matlab*, 3rd ed. Boca Raton, FL: CRC Press, 2012.
- [16] S. M. Kay, *Fundamentals of Statistical Signal Processing*, 1st ed. Upper Saddle River, NJ: Prentice-Hall, 1998.
- [17] *Manual on Classification of Motor Vehicle Traffic Accidents*, ANSI D16.1, 2007. [Online]. Available: <http://standards.globalspec.com/std/1712071/ansi-d16-1>
- [18] American Association of State Highway Officials, "A policy on geometric design of highways and streets," American Association of State Highway Officials, Washington, DC, 2001.
- [19] V. Carotenuto, A. De Maio, C. Clemente, J. J. Soraghan, and G. Alfano, "Forcing scale invariance in multipolarization SAR change detection," *IEEE Trans. On Geosci. And Remote Sens.*, vol. 54, pp. 36–50, 2016.
- [20] I. Stojanovic and L. Novak, "Change detection experiments using gotcha public release data," in *Proceedings of SPIE Algorithms for Synthetic Aperture Radar Imagery*, Baltimore, MD, 2013, vol. 8746.

## **INITIAL DISTRIBUTION LIST**

1. Defense Technical Information Center  
Ft. Belvoir, Virginia
2. Dudley Knox Library  
Naval Postgraduate School  
Monterey, California